Design of a Model Propulsor for a Boundary Layer Ingesting Aircraft

by

Adam D. Grasch

Submitted to the Department of Aeronautics and Astronautics
in partial fulfillment of the requirements for the degree of

Master of Science in Aeronautics and Astronautics

at the

MASSACHUSETTS INSTITUTE OF TECHNOLOGY

September 2013

Author ....
Department of Aeronautics and Astronautics
August 26, 2013

Certified by.......... ....
Edward M. Greitzer
H.N. Slater Professor of Aeronautics and Astronautics
Thesis Supervisor

Accepted by ....
Eytan H. Modiano
Professor of Aeronautics and Astronautics
Chair, Graduate Program Committee

Design of a Model Propulsor for a Boundary Layer Ingesting Aircraft

by

Adam D. Grasch

Submitted to the Department of Aeronautics and Astronautics
on August 26, 2013, in partial fulfillment of the
requirements for the degree of
Master of Science in Aeronautics and Astronautics

Abstract

This thesis presents contributions to the analysis and design of propulsion simulators for 1:11 and 1:4 scale model wind tunnel investigations of an advanced civil transport aircraft with boundary layer ingestion (BLI). The electrically powered single-stage propulsors represent the ultra-high bypass ratio turbofan engines on a full-scale conceptual aircraft previously designed at MIT. Powered models will use these propulsors in both podded and boundary layer ingesting configurations to allow back-to-back assessment of BLI benefit. The thesis gives a description of work on propulsion system scaling, nacelle and flowpath aerodynamic optimization, mechanical design of the propulsor and characterization of the propulsor electric motors, all in support of the wind tunnel experiments. Explicit definition is given of those designs that meet the requirements of the program as well as those in which there are items still to be addressed.

Thesis Supervisor: Edward M. Greitzer
Title: H.N. Slater Professor of Aeronautics and Astronautics

Acknowledgments

This work was completed under the support of the Air Force Office of Scientific Research (AFOSR) through the National Defense Science & Engineering Graduate Fellowship (NDSEG) Program. The N+3 project in general is generously supported by the NASA Fixed Wing Project. First and foremost, I would like to thank Prof. Ed Greitzer for his guidance and mentorship; it has been an honor. I would also like to gratefully acknowledge the support and assistance of numerous employees of the N+3 team partners Aurora Flight Sciences and Pratt & Whitney, particularly Jeremy Hollman, David Kordonowy, Roedolph Opperman, Benjamin Smith and Wes Lord. Many thanks also to Blake Moffitt of the United Technologies Research Center (UTRC), and Prof. Mark Drela of MIT for his wisdom and guidance. I would also like to thank my fellow members of the MIT N+3 team for their many contributions to this work and to the project in general, in particular Michael Lieu, Nina Siu, Alex Espitia, Alejandra Uranga, Neil Titchener, Arthur Huang, Chris Maynor and David Hall.

The other members of the MIT Gas Turbine lab deserve special thanks also, for many late night discussions of problem sets and research questions. I am particularly grateful to Anjaney Kottapalli, Steve Mazur, Max Brand and Vishnu Jyothindran. I also owe a debt of gratitude to my former mentors at Duke and in the UK, Profs. Earl Dowell, Mark Lowenberg and Michael Friswell, for the time and effort spent encouraging and preparing me for graduate school and a career in aerospace engineering. Lastly I want to thank my family for their incredible support of my educational and intellectual goals throughout my life, and especially my fiancée Jessica Morrison, for somehow having the patience to put up with me through the graduate school process and everything else that life has thrown our way. I am grateful to you all.

Contents

List of Figures

List of Tables

Nomenclature

Latin Characters

A	Area
c	Chord length
c_p	Specific heat capacity
C_p	Pressure coefficient
C_T	Thrust coefficient
C_x	Flow velocity at fan face
D	Diameter
$\mathcal{D}$	Area-weighted flow disturbance magnitude
D_c	Duty-cycle
d_h	Hydraulic diameter
$^{e}/_{D}$	Normalized pipe roughness
F	Force
H	Boundary layer shape parameter
h	Heat transfer coefficient
h_t	Stagnation enthalpy per unit mass
$^{H}/_{T}$	Fan hub to tip ratio
i	Electrical current
K	Screen pressure drop coefficient
k	Thermal conductivity
k_{loss}	ESC efficiency loss coefficient
K_Q	Motor torque constant

K_r	Radial bearing stiffness
$\dot{m}$	Mass flow
N	Disturbance growth exponent
N_{crit}	Critical disturbance growth exponent for boundary layer transition
Nu	Nusselt number
P	Power
p	Pressure
Pr	Prandtl number
Q_m	Motor torque
$\dot{Q}$	Heat flux
q	Dynamic pressure
r	Radial position coordinate
Re	Reynolds number
s	Screen solidity
T	Temperature
t_1	Motor efficiency temperature coefficient
u	Streamwise velocity
$\mathbf{u}'$	Velocity perturbation
U_{tip}	Fan tip speed
V	Velocity
v	Electrical voltage
V'_∞	Equivalent inlet velocity for BLI
$\dot{W}$	Motor Power
$\vec{X}$	Vector of design variables
x	Streamwise or axial position coordinate
y	Position coordinate normal to streamlines
Z	Number of rolling elements in a bearing

Greek Characters

α	Angle of attack
γ	Ratio of specific heats
Δ	Change
δ^*	Boundary layer displacement thickness
$\delta_{0.95}$	95% boundary layer thickness
η	Efficiency
θ^*	Kinetic energy thickness
$\mathcal{K}$	Net normalized kinetic energy defect (summed across wakes)
κ	Normalized kinetic energy defect
λ	Darcy-Weisbach friction coefficient
ν	Kinematic viscosity
ρ	Flow density
σ	Standard deviation
ϕ	Flow coefficient
ψ	Stage loading coefficient
Ω	Rotational speed
ω	Frequency

Subscripts

b	Ball bearing
c	Cooling
$calc$	Calculated
e	Boundary layer edge
f	Fan, isentropic
for	Forward
h	Hub

j	Jet
m	Motor
$meas$	Measured
n	Natural (frequencies)
nom	Nominal
p	Propulsive
ref	Reference
rev	Reverse
$spec$	Specified
t	Stagnation
θ	Circumferential

Propulsor Stations

∞	Freestream
12	Fan face
13	Bypass flow just downstream of fan
18	Nozzle

Abbreviations

BLDC	Brushless DC electric motor
BLI	Boundary layer ingestion
CFD	Computational fluid dynamics
CNC	Computer numeric control
COTS	Commercial off-the-shelf
DC	Direct current
DoE	Design of experiments

EMF	Electromotive force
EO	Engine order
ESC	Electronic speed controller
FDM	Fused deposition modeling
FEA	Finite element analysis
FFT	Fast-Fourier transform
IBLT	Interacting boundary layer theory
LaRC	NASA Langley Research Center
MTFLOW	Multi-passage throughflow code
NACA	National Advisory Committee for Aeronautics
NASA	National Aeronautics and Space Administration
PWM	Pulse-width modulation
TASOPT	Transport aircraft system optimization code
UAV	Unmanned aerial vehicle
WBWT	Wright Brothers Wind Tunnel

Chapter 1

Introduction

The NASA Fixed Wing Project under the Aeronautics Research Mission Directorate is developing concepts and tools for future transport aircraft with significant reductions in fuel burn, noise and environmental impact relative to today's standard [1]. A roadmap of target performance improvements has been laid out over several generations of passenger aircraft, from N+1 (~2015) to N+3 (~2025). The challenge presented by this third-generation aircraft has led to a partnership between MIT, Aurora Flight Sciences and Pratt & Whitney to design and assess aircraft and propulsion concepts appropriate for the N+3 goals. This partnership is supported by NASA, which is also working as a close collaborator.

The N+3 goals are specified in relation to current aircraft. Among the most ambitious are a 60% reduction in fuel burn and 71 dB reduction in noise compared to the Boeing 737-800 [1] [1]. A baseline aircraft known as the 'D8' was designed to these specifications by Drela using his Transport Aircraft System Optimization (TASOPT) code [2] which makes use of the 'double-bubble' fuselage concept, seen in Fig. 1 [3]. The double-bubble fuselage has a tension web running the length of the cabin allowing the creation of a pressure vessel with lower hoop stress concentrations than an elliptical cross-section and simplifying structural design for cabin pressurization at altitude. This configuration widens the fuselage relative to conventional tube-and-wing

---

[1] The N+3 Phase I fuel reduction goal was 70% relative to the 737-800. This has since been modified.

aircraft, allowing increased carryover lift and therefore shrinking the wing [3]. The fuselage is shaped such that the center-of-lift during cruise is forward of the aircraft center-of-gravity, giving a nose-up moment. This reduces the down-force needed at the aft of the aircraft and shrinks the horizontal tail.

The engines are moved to above the rear of the fuselage in a boundary layer ingesting (BLI) configuration whose propulsive benefits will be discussed subsequently. Such an engine configuration has a number of additional benefits, including a reduction in the structural loads carried in the wing box and the engine-out moment. These two effects reduce the wing weight and shrink the vertical tail, respectively. The aircraft is designed to cruise more slowly than the baseline 737-800, at Mach 0.72 rather than 0.80, allowing the wing to be unswept and reducing drag. Additional benefits come from BLI engine technology and the use of advanced composite materials, which combine to give an estimated system-level performance improvement near that specified by the N+3 project goals. For more details on the philosophy behind this aircraft design see the paper by Drela [4].

In a conventional passenger aircraft configuration, propulsors are located well enough away from the fuselage and wing to create a distinct momentum excess in the wake in the form of a jet and a momentum defect from the viscous wakes of the fuselage, both of which have an associated kinetic energy. A benefit can be gained by the stacking of the two as seen in Fig. 1-2 [5]. In a BLI configuration, aircraft propulsors ingest some or all of the fuselage boundary layer, with the net effect of 'filling-in' the wake defect. The effect of BLI is to reduce the required power input to the flow from the propulsor, yielding a net fuel savings. A useful framework for the understanding of this effect can be from the perspective of a power-balance, as described by Drela [5].

Fuel savings from BLI is an issue of active research and one of the major goals of the MIT, Aurora Flight Sciences and Pratt & Whitney N+3 project. Preliminary computational results show fuel savings of about 7% for the present geometries [6] (although this idealized benefit may be reduced by lower fan efficiency due to operation in distortion, as well as other effects associated with application to a real aircraft).

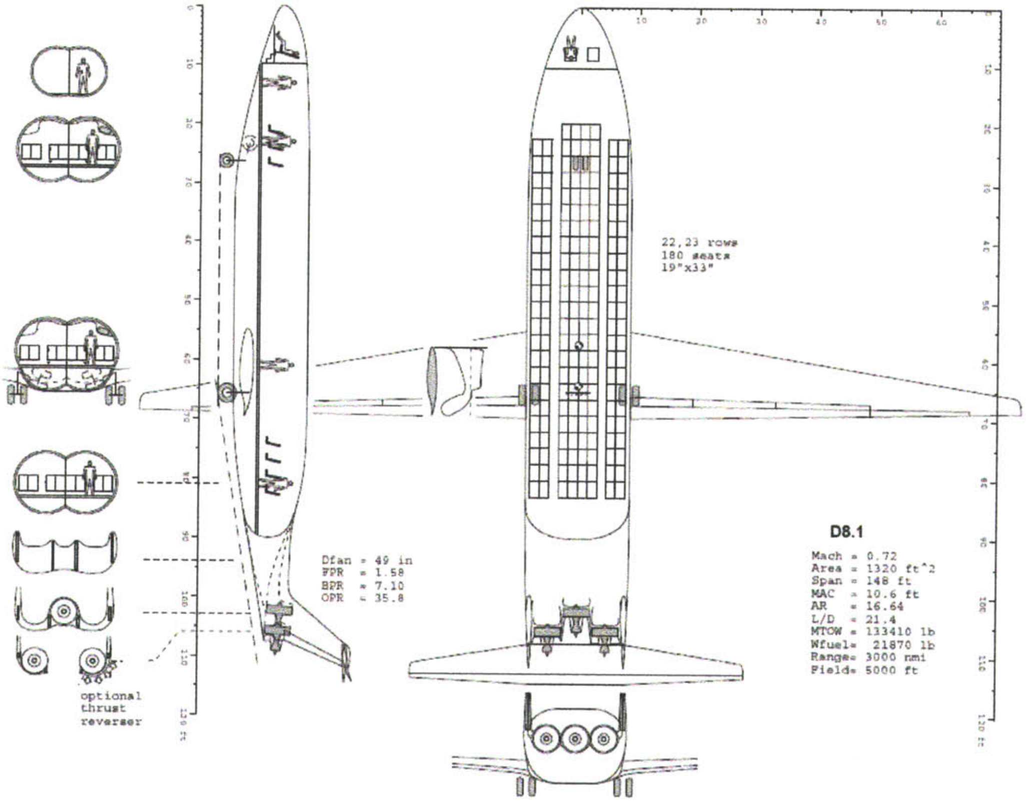

Figure 1-1: D8 aircraft concept with 'double-bubble' fuselage.

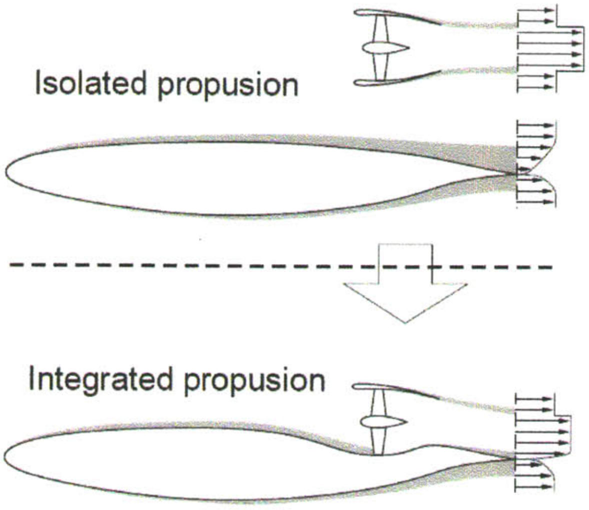

Figure 1-2: 'Filling in' of the wake as a result of boundary layer ingestion.

To better define the realizable benefit of BLI, wind tunnel models of the D8 are being designed and tested at several scales. Podded and integrated configurations, as sketched in Fig. 1-3, are being examined in the MIT Wright Brothers Wind Tunnel (WBWT) and in the NASA Langley Research Center (LaRC) 14'×22' tunnel. The engines are represented by ducted fans driven by electric motors. The integrated configuration includes BLI. The podded configuration has the same wing and forward fuselage as the integrated configuration, but the aft section of the aircraft body supports two engines located on pylons of a length sufficient to aerodynamically decouple the propulsor and fuselage and thus has no BLI. The turbomachinery is kept the same in the two configurations, with the nacelle outer surface changed. The goal is to allow direct comparison between the propulsive power required to simulate cruise in the two configurations.

One set of propulsors have been designed and constructed for a 1:11 scale model using commercial off-the-shelf (COTS) ducted fans. Experiments with 'custom-designed propulsors' are also planned at the 1:11 and 1:4 scales. These propulsors are intended to operate at a propulsive efficiency that corresponds more closely to the full scale

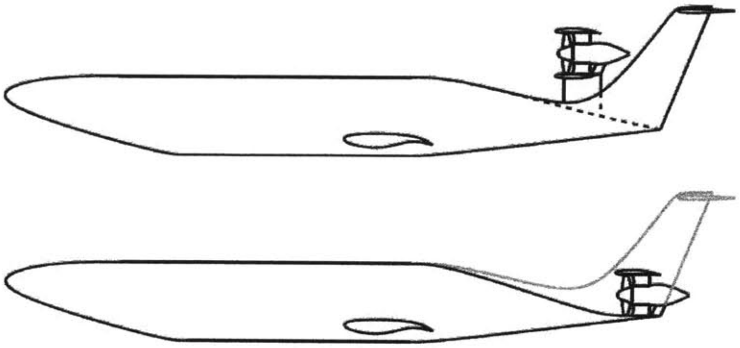

Figure 1-3: Podded (above) and integrated (below) wind tunnel models.

design. The 1:11 scale custom propulsor also serves as a prototype for the 1:4 scale, allowing risk reduction for the larger test and providing a back-to-back comparison of the aircraft with different turbomachinery [7].

The structural, aerodynamic, thermal and electrical design and analysis of the custom scaled propulsors is the main subject of this thesis. Some contributions are made to the COTS propulsor and power system as well. The work covers aspects of models at both 1:11 and 1:4 scales.

A primary constraint on the propulsor design has been the selection of appropriate electric motors. Scaling arguments for the required motor speed and shaft power will therefore be presented in addition to predictions of motor operating condition and efficiency. Results from dynamometer testing carried out at MIT and work on thermal management will also be discussed, as will aerodynamic optimization of the propulsor nacelles and internal flowpath. The preliminary mechanical design of a 1:11 scale custom propulsor will be described, as will the development of a modified wind tunnel test section for the testing of future propulsors at 1:4 scale.

Chapter 2

Propulsion System Sizing and Electric Motor Selection

The electric motors driving the powered-model propulsors impose major constraints on the overall test article design. Motors are available in a wide range of speed and power levels and in a variety of configurations. In general the physical size of the motor tends to increase with increasing shaft power, and it is important to determine which motors capable of providing the desired output can be found in a size suitable for our custom 1:11 and 1:4 scale model propulsors. Availability of such motors is a determinant of the model scale and attainable wind tunnel test speed.

Replicating full-scale Mach and Reynolds numbers is impossible given size and velocity constraints, and the use of scaled models and low-speed wind tunnels forces a choice of non-dimensional model scaling parameters. A subset of parameters must be selected which is sufficient to define the model and propulsion system in a relevant manner. Two such subsets are considered here. The first, which works from a high-level vehicle standpoint, matches full-scale values for the flow coefficient $\phi \equiv {}^{C_x}/_{U_{tip}}$, work coefficient $\psi \equiv {}^{\Delta h_t}/_{U_{tip}^2}$ and overall propulsive efficiency η_p. The second, which is based on the turbomachinery, matches ϕ, ψ and the ratio of fan-face to freestream velocity ${}^{C_x}/_{V_\infty}$ [8]. The former is the perspective adopted, but it is shown that the two methods give similar results and agree with a power-balance scaling analysis as well [9]. This indicates that motor selection is not sensitive to the choice of scaling method.

The aim is to provide a scaling which allows motor selection to proceed and model scale to be set, with the understanding that a subsequent, more detailed analysis may be used to fine-tune operating points for wind tunnel tests. The scaling exercise is carried out assuming operation of the propulsor in the integrated configuration because the variation in speed and power requirement associated with the podded configuration is small enough not to affect motor selection or model scale [9]. Some thermal considerations will be addressed as well after suitable motors have been specified.

2.1 Matching ϕ, ψ and η_p

ϕ, ψ and η_p represent one subset of the available scaling parameters which is sufficient to define the model and propulsion system. This admits direct comparisons between the scale model and full-scale aircraft performance.

The sizing analysis assumes as fixed the parameters listed in Table 2.1. The fan diameter values represent a geometric scaling of the D8.6 full-scale design [1], and the non-dimensional turbomachinery parameters are estimated based on full-scale values as described by Lord [10], which largely informs the method of this analysis. The nominal 1:11 and 1:4 scale freestream tunnel velocities represent 60% and 70% of the NASA Langley 14'×22' wind tunnel maximum speed, respectively. The propulsive efficiency is defined by

$$\eta_p = \frac{F V_\infty}{\dot{W}}, \tag{2.1}$$

$$\eta_p = \frac{\cancel{\dot{m}} \left(V_j - V'_\infty \right) V_\infty}{\cancel{\dot{m}} \Delta h_t}, \tag{2.2}$$

where F is thrust. Eq. 2.2 gives an expression for V_j as a function of the stagnation enthalpy rise per unit mass Δh_t, the equivalent inlet velocity V'_∞, and fixed parameters. The equivalent inlet velocity V'_∞ is determined from the BLI inlet pressure loss

Parameter	1:11	1:4	Definition
ϕ	0.625		Flow coefficient, ${}^{C_x}/_{U_{tip}}$
ψ	0.290		Work coefficient, ${}^{\Delta h_t}/_{U_{tip}^2}$
η_p	0.806		Propulsive efficiency
η_f	0.950		Isentropic fan efficiency
${}^{H}/_{T}$	0.365		Hub to tip ratio
p_∞	101.4		Atmospheric pressure (sea level) [kPa]
T_∞	288.2		Ambient temperature (sea level) [K]
${}^{(p_\infty - p_{t,12})}/_{q_\infty}$	0.170		BLI inlet pressure loss coefficient
${}^{\Delta p_{t,duct}}/_{\Delta p_{t,fan}}$	0.050		Fan duct loss coefficient
V_∞	63.6	74.2	Nominal tunnel velocity [m/s]
D	14.4	39.7	Fan outer diameter [cm]

Table 2.1: Nominal parameter values for 1:11 and 1:4 scale models.

coefficient according to

$$V_\infty' = V_\infty \left[1 - \left(\frac{p_\infty - p_{t,12}}{q_\infty}\right)\right]^{1/2} . \tag{2.3}$$

Station labeling follows Fig. 2.1 which is in line with industry practice. We need a second expression for V_j as a function of Δh_t and the fixed parameters to close the solution. We can solve for the fan inlet stagnation pressure as

$$p_{t,12} = p_\infty - \frac{1}{2}\rho V_\infty^2 \left(\frac{p_\infty - p_{t,12}}{q_\infty}\right) . \tag{2.4}$$

We assume that the BLI inlet pressure loss scales with dynamic head and can be represented by the coefficient $\left(\frac{p_\infty - p_{t,12}}{q_\infty}\right) \approx 0.17$ [10]. The temperature rise across the fan is

$$\Delta T_t = \frac{\Delta h_t}{c_p} , \tag{2.5}$$

which determines the temperature ratio and allows the fan pressure ratio to be found by

$$\frac{p_{t,13}}{p_{t,12}} = 1 + \eta_f \left[\left(\frac{T_{t,13}}{T_{t,12}}\right)^{\gamma/\gamma-1} - 1\right] . \tag{2.6}$$

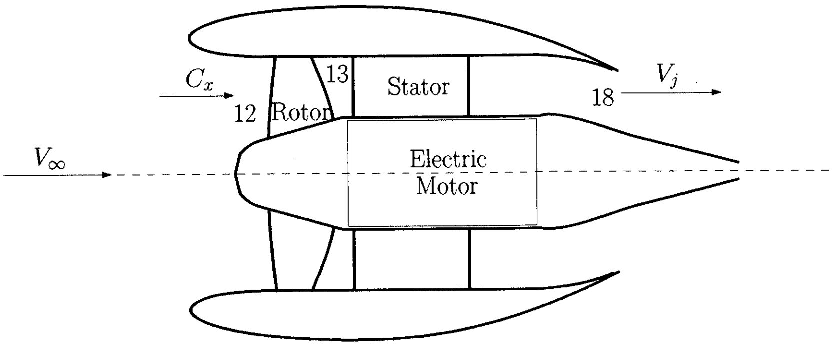

Figure 2-1: Propulsor station and velocity labeling.

The fan nozzle stagnation pressure is then

$$p_{t,18} = p_{t,12} \left[\left(1 - \frac{\Delta p_{t,duct}}{\Delta p_{t,fan}} \right) \frac{p_{t,13}}{p_{t,12}} + \frac{\Delta p_{t,duct}}{\Delta p_{t,fan}} \right] , \tag{2.7}$$

where ${}^{\Delta p_{duct}}/_{\Delta p_{fan}} \approx 0.05$ [10]. Another expression for V_j can now be found from assuming incompressible flow and nozzle static pressure equal to the freestream,

$$V_j = \left[V_\infty^2 + \frac{2}{\rho} \left(p_{t,18} - p_\infty \right) \right]^{1/2} , \tag{2.8}$$

where $p_{t,18}$ is a function of Δh_t. Eqs. 2.8 and 2.2 are two equations with two unknowns, Δh_t and V_j, which can be solved numerically. The flow area at the fan face is

$$A_{12} = \frac{1}{4} \pi D^2 \left[1 - \left({}^{H}/_{T} \right)^2 \right] , \tag{2.9}$$

and the mass flow is

$$\dot{m} = \rho C_x A_{12} . \tag{2.10}$$

Tip speed and motor power are given by

$$U_{tip} = \sqrt{\frac{\Delta h_t}{\psi}} , \tag{2.11}$$

and

$$\dot{W} = \dot{m}\Delta h_t\,. \tag{2.12}$$

The fan speed is

$$\Omega = \frac{U_{tip}}{\pi D}\,. \tag{2.13}$$

Eqs. 2.1 - 2.13 allow solution for motor power $\dot{W}$ and speed Ω as a function of the specified parameters. For the values listed in Table 2.1, we obtain a 2.0 kW motor operating at 11.5 krpm for the 1:11 scale model. For the 1:4 scale model 25.1 kW and 4.9 krpm are suggested.

In reality, D and V_∞ may vary up to perhaps ±10% of their nominal values and we wish to pick D in a manner which will allow access to a high tunnel speed at achievable values of $\dot{W}$ and Ω. Towards this end it is worthwhile to determine the sensitivity of the results to small changes in these and other parameter values.

2.1.1 Sensitivities

Normalized sensitivities may be computed about the nominal operating points given in Table 2.1 according to

$$\frac{\Delta J^*/J^*}{\Delta x^*/x^*} = \frac{x^*}{J(x^*)}\left(\frac{\partial J}{\partial x}\right)\bigg|_{x^*}\,, \tag{2.14}$$

where $\frac{\partial J}{\partial x}$ is determined using second-order centered finite differencing [11]

$$\frac{\partial J}{\partial x} = \frac{J(x+\Delta x) - J(x-\Delta x)}{2\Delta x}\,. \tag{2.15}$$

The sensitivities in Table 2.2 indicate the effect of a percent change in a given parameter value on $\dot{W}$ and Ω and can be understood with reference to Eqs. 2.1 - 2.13. The sensitivities are almost unchanged with model scale.

It can also be seen from Table 2.2 that the sensitivity to the loss parameters $(p_\infty - p_{t,12})/q_\infty$ and $\Delta p_{t,duct}/\Delta p_{t,fan}$ is small in comparison to the other parameters, so precision in these values is not strictly necessary. The motor requirements are sensitive

	1:11		1:4	
	$\dot{W}$	Ω	$\dot{W}$	Ω
D	2.00	-1.00	2.00	-1.00
V_∞	3.08	1.03	3.14	1.05
$^{\mathrm{H}}/_{\mathrm{T}}$	-0.31	0	-0.31	0
ϕ	1.00	0	1.00	0
ψ	-0.50	-0.50	-0.50	-0.50
η_p	-9.76	-3.25	-9.89	-3.30
η_f	8.22	2.74	8.29	2.76
p_∞	8.22	2.74	8.32	2.78
T_∞	-8.27	-2.76	-8.40	-2.80
$(p_\infty - p_{t,12})/q_\infty$	0.62	0.21	0.64	0.21
$\Delta p_{t,duct}/\Delta p_{t,fan}$	-0.41	-0.14	-0.45	-0.15

Table 2.2: Percent change in $\dot{W}$ or Ω per percent change in parameter value when $\eta_p = 0.806$.

to the isentropic fan efficiency and to the full-scale value of propulsive efficiency.

2.2 Matching ϕ, ψ and C_x/V_∞

We also examine the effect of matching the full-scale value of $C_x/V_\infty = 0.871$ rather than η_p. This replicates the capture area and overall turbomachinery characteristic of the full-scale aircraft.

The primary difference between this method and that of Section 2.1 is that Δh_t is known immediately from

$$U_{tip} = \frac{V_\infty}{\phi}\left(\frac{C_x}{V_\infty}\right), \tag{2.16}$$

$$\Delta h_t = \psi U_{tip}^2 . \tag{2.17}$$

A_{12}, $\dot{m}$, $\dot{W}$ and Ω can be found from Eqs. 2.9, 2.10, 2.12 and 2.13 as before. The area ratio $A_{18}/A_{12} = C_x/V_j$ can be found from continuity. When values from Table 2.1 are inserted into these equations, similar motors are specified as in the previous analysis. Table 2.3 compares the results of the two methods.

Variable	1:11		1:4	
	η_p	${}^{C_x}/_{V_\infty}$	η_p	${}^{C_x}/_{V_\infty}$
$\dot{W}$ [kW]	2.0	2.2	25.1	26.4
Ω [krpm]	11.51	11.76	4.90	4.98
${}^{C_x}/_{V_\infty}$	0.852	0.871	0.856	0.871
η_p	0.806	0.800	0.806	0.802
${}^{V_j}/_{V_\infty}$	1.345	1.362	1.350	1.363
${}^{A_{18}}/_{A_{12}}$	0.633	0.640	0.634	0.639

Table 2.3: Comparison of propulsion sizing methods.

2.2.1 Sensitivities

Normalized sensitivities for this second analysis are shown in Table 2.4. Sensitivities to D, V_∞ and ${}^{H}/_{T}$ are similar to those presented in Table 2.2. The sensitivities to ϕ and ψ are different, however, because of the differing approaches to determining Δh_t. Agreement between the two methods is thus limited to a certain range of ϕ and ψ values for our current choice of other parameter values. The effects of these parameters can be portrayed by combining Eqs. 2.9, 2.10, 2.12, 2.13, 2.16 and 2.17 into two equations for $\dot{W}$ and Ω:

$$\dot{W} = \frac{\pi\rho\left({}^{C_x}/_{V_\infty}\right)^3 V_\infty^3 D^2\left[1-\left({}^{H}/_{T}\right)^2\right]\psi}{4\phi^2}, \tag{2.18}$$

$$\Omega = \frac{\left({}^{C_x}/_{V_\infty}\right)V_\infty}{\pi D\phi}. \tag{2.19}$$

Eqs. 2.18 and 2.19 show that $\dot{W} \sim V_\infty^3 D^2$ and $\Omega \sim {}^{V_\infty}/_{D}$, so increasing model scale requires larger motor power for the same V_∞ but a lower motor speed. Increasing model scale allows room for a larger diameter motor, because the constraint on motor size is that the outer diameter of the electric motor is small enough to allow the desired flow area at the fan nozzle, A_{18},

$$D_{motor} \leq D\left[1-\frac{A_{18}}{A_{12}}+\frac{A_{18}}{A_{12}}\left(\frac{H}{T}\right)^2\right]^{1/2}. \tag{2.20}$$

	1:11		1:4	
	$\dot{W}$	Ω	$\dot{W}$	Ω
D	2.00	-0.98	2.00	-1.00
V_∞	2.87	0.98	3.08	1.11
$^{\mathrm{H}}/_{\mathrm{T}}$	-0.31	0	-0.31	0
$^{C_x}/_{V_\infty}$	3.00	0.98	3.00	1.00
ϕ	-2.00	-0.98	-2.00	-1.00
ψ	1.00	0	1.00	0

Table 2.4: Percent change in $\dot{W}$ or Ω per percent change in parameter value when $^{C_x}/_{V_\infty} = 0.871$.

For the D and $^{H}/_{T}$ in Table 2.1 and $^{A_{18}}/_{A_{12}} \approx 0.64$, the maximum motor diameters are 9.7 and 26.4 cm.

2.3 Motor Selection

2.3.1 1:11 Scale

Once the speed and shaft power of the electric motors for the two models are found, we can select suitable motors which satisfy the size constraint in Eq. 2.20. Fig. 2-2 provides a framework for visualizing changes in the four variables $\dot{W}$, Ω, D and V_∞ and the corresponding effect on motor selection for the 1:11 scale model. Contours of $^{V_\infty}/_{V_{max}}$ are given in the figure with shaft power and motor speed on the axes. Model scale varies across the plot, but the line of constant $D = D_{nom}$ is shown with ±10% bands. For a given $(\dot{W}, \Omega)$ point on a line of constant D, the tunnel velocity necessary to match the full scale value of η_p can be read from Fig. 2-2. The nominal operating point determined in the analysis of Section 2.1 is also marked by the red triangle. For an increase in D at constant V_∞, the operating point moves to the left along the 60% tunnel velocity contour, giving higher motor power and lower motor speed.

Feasible regions for three commercially available electric motors are to the lower left of the black constraint lines. The upper constraints are set by the motors' maximum power outputs [12], and the right-hand bounds are constraints on minimum

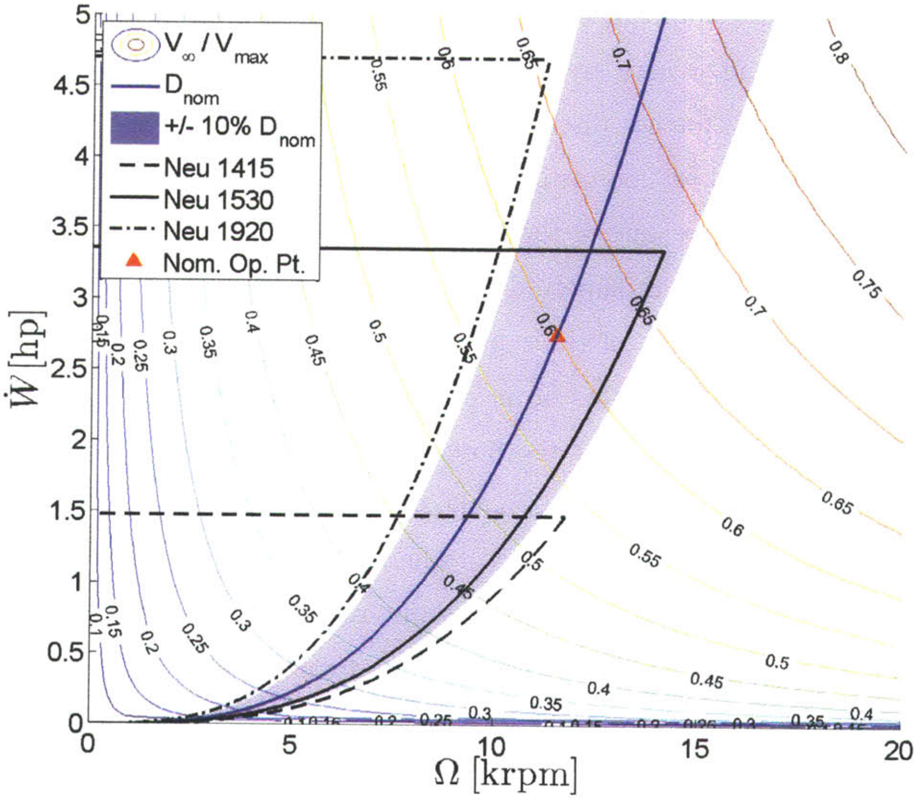

Figure 2-2: Contours of V_∞/V_{max} vs. $\dot{W}$ and Ω for 1:11 scale, $\eta_p = 0.806$. The line of constant $D = D_{nom}$ is plotted with $\pm 10\%$ bands. Feasible regions for three candidate motors are to the lower left of the black constraint lines.

fan size set by the motor diameter and Eq. 2.20. A 3/8" margin has been allowed to account for cooling and structure inside the propulsor core.

The nominal operating point is attainable using the NeuMotors 1530. Additional tunnel speed could be allowed by using the higher power 1920 model, but this would require an increase in fan diameter (and hence overall model scale) of about 5%. The smaller 1415 motor could be selected but if so it could not be operated at higher than about 48% of the maximum tunnel speed without decreasing D.

The motors presented here are brushless DC electric motors, whose operation and characteristics are further discussed in Chapter 5. They have been shown to outperform conventional DC motors in terms of speed, torque, reliability and life [13]. Such motors represent the state of the art for small unmanned aerial vehicle (UAV) propulsion [14], whose power supply demands are similar to those of our powered wind tunnel models, and are of the type used in the COTS propulsor. The main conclusion is that suitable motors of an appropriate type exist in the desired size, speed and power range, and that the potential (5%) increase in V_∞ allowed by a higher power motor is not significant enough to warrant a change in model scale.

The above conclusions hold regardless of whether η_p or ${}^{C_x}/_{V_\infty}$ are chosen for scaling. This can be seen from Fig. 2-3, in which results from the two analyses are overlaid. Along the red tunnel speed contours, ϕ, ψ and η_p are at full-scale values while along the blue contours ${}^{C_x}/_{V_\infty}$ is matched rather than η_p. At fixed model scale, the only alteration required to match ${}^{C_x}/_{V_\infty}$ rather than η_p is to run the electric motor about 2.2% faster.

2.3.2 1:4 Scale

Fig. 2-4 replicates Fig. 2-2 for the 1:4 scale test article. Three potential motor choices are shown, with the feasible regions to the lower left of the bounding lines. The 9 in. diameter AC-50 from High Performance Electric Vehicle Systems (HPEVS) [15] is one suitable choice, but if a smaller diameter motor is desired to allow more room for structural components or cooling in the centerbody of the propulsion simulator, the 8 in. diameter DC 203-06-4001 [16] motor can also be used, although it restricts

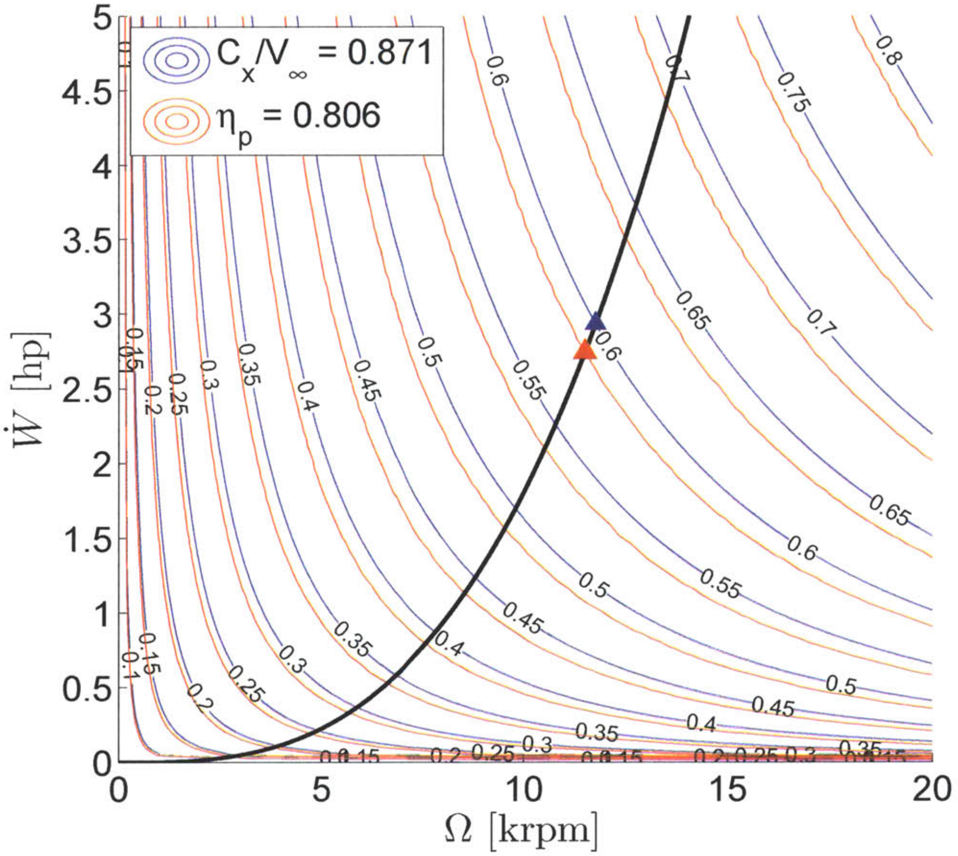

Figure 2-3: Comparison of constant ${C_x}/{V_\infty}$ and η_p models, 1:11 scale.

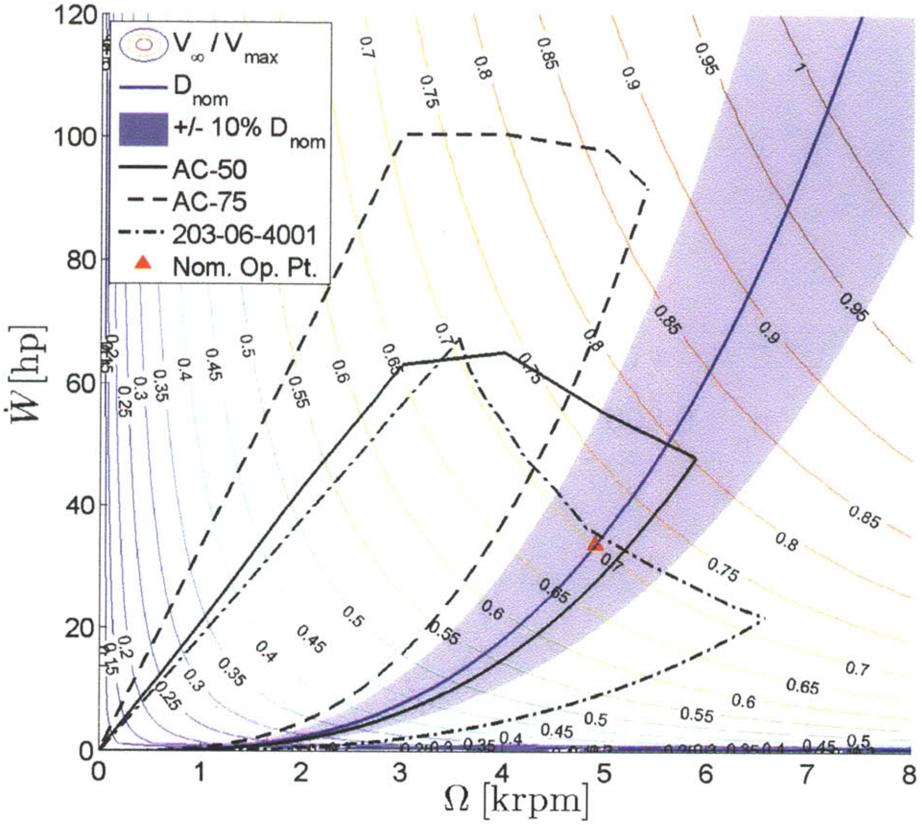

Figure 2-4: Contours of V_∞/V_{max} vs. $\dot{W}$ and Ω for 1:4 scale, $\eta_p = 0.806$. The line of constant $D = D_{nom}$ is plotted with ±10% bands. Feasible regions for three candidate motors are to the lower left of the black constraint lines.

testing to lower tunnel speed.

If testing is desired above about 78% of the maximum LaRC tunnel velocity, a more powerful motor such as the AC-75 [15] is required which has a correspondingly larger diameter. The AC-75 is too large to fit in the 1:4 model at the nominal scale, and requires an increase in fan diameter of about 15%. Again the potential benefit does not appear to warrant a change in model scale.

2.4 Thermal Management

A method of waste heat removal, via either air or water, is needed for the electric motors to allow sufficient operation times without overheating. For air cooling, core flow is bled through the centerbody from an inlet at the fan face and exhausted through a downstream port. For water cooling, a waterjacket is required, encasing all or part of the motor casing, along with tubing for water to be pumped from outside the model, into the waterjacket and then back out through ducting channels in the aircraft fuselage. Both methods are examined below.

The heat flux requirement can be estimated from the motor efficiency given by

$$\eta_m = \frac{\dot{W}}{\dot{W}_{in}} \,. \tag{2.21}$$

We assume $\eta_m = 0.80$ as a conservative value for the sizing calculation, although this varies with operating point and other parameters [14]. The excess heat flux $\dot{Q}$ is

$$\dot{Q} = \dot{W}\left(1 - \eta_m\right) \,. \tag{2.22}$$

2.4.1 Air Cooling

Heat is removed from the motor by both natural and forced convection, but the former is only a few percent of latter [17] and we neglect it here. The heat removal is

$$\dot{Q} = hA\Delta T \,, \tag{2.23}$$

where the surface area of heat removal A neglects the endcaps of the cylindrical motor, ΔT is the temperature difference between the motor frame and the surrounding flow, and the heat transfer coefficient h is determined from the thermal conductivity of air

k and the Nusselt number as below:

$$A = (0.0254^2)\pi D_m L_m\,, \tag{2.24}$$

$$\Delta T = T_{frame} - T_{t,0} - \Delta T_{fan}\,, \tag{2.25}$$

$$h = \left(\frac{k}{D_m}\right) Nu\,. \tag{2.26}$$

The Nusselt number is estimated from [18]

$$Nu = 0.036 Re_L^{4/5} Pr^{1/3}\,. \tag{2.27}$$

The relevant air properties k, Pr and viscosity ν are evaluated at atmospheric pressure and the film temperature defined by

$$T_{film} = \frac{1}{2}\left(T_{frame} + T_{t,0} + \Delta T_{fan}\,.\right) \tag{2.28}$$

Eqs. 2.23 - 2.28 can be solved for a constraint on the Reynolds number and hence on the required cooling flow velocity V_c,

$$V_c \geq \left[\frac{\dot{W}\left(1-\eta_m\right)\nu^{4/5}}{0.036\pi k \Delta T Pr^{1/3} L_m^{9/5}}\right]^{5/4}\,. \tag{2.29}$$

An additional constraint comes from the requirement that sufficient mass flow of air is bled through the core to accept the generated waste heat. This minimum mass flow is

$$\dot{m} \geq \frac{\dot{Q}}{c_p \Delta T}\,, \tag{2.30}$$

which becomes a constraint on V_c according to

$$V_c \geq \frac{\dot{Q}}{\rho A_c c_p \Delta T}\,. \tag{2.31}$$

In Eq. 2.31, A_c is the flow area inside the core gap between the motor skin and the inner surface of the hub, given by $\pi/4\,(D_h^2 - D_m^2)$. For the 1:11 scale model $D_h \approx 3$

in and $D_m = 1.5$ in (NeuMotors 1530); at 1:4 scale $D_h \approx 10$ in and $D_m = 9$ for the AC-50. For both cases the mass flow constraint is dominated by the convective cooling constraint, and V_c is set by Eq. 2.29. The required cooling flow varies with operating point as shown in Figs. 2-5 and 2-6. η_m will also vary with operating point, but this effect is not captured in Figs. 2-5 and 2-6.

The required core airflow is either about 30% or about 50% of the wind tunnel freestream velocity, depending on model scale. The design of an intake system which will draw sufficient cooling flow into the core is not trivial, and indeed the losses along such an internal flow path can prove high enough that it is difficult to attain the proper throughflow velocities. For this reason water-cooling is an attractive alternative.

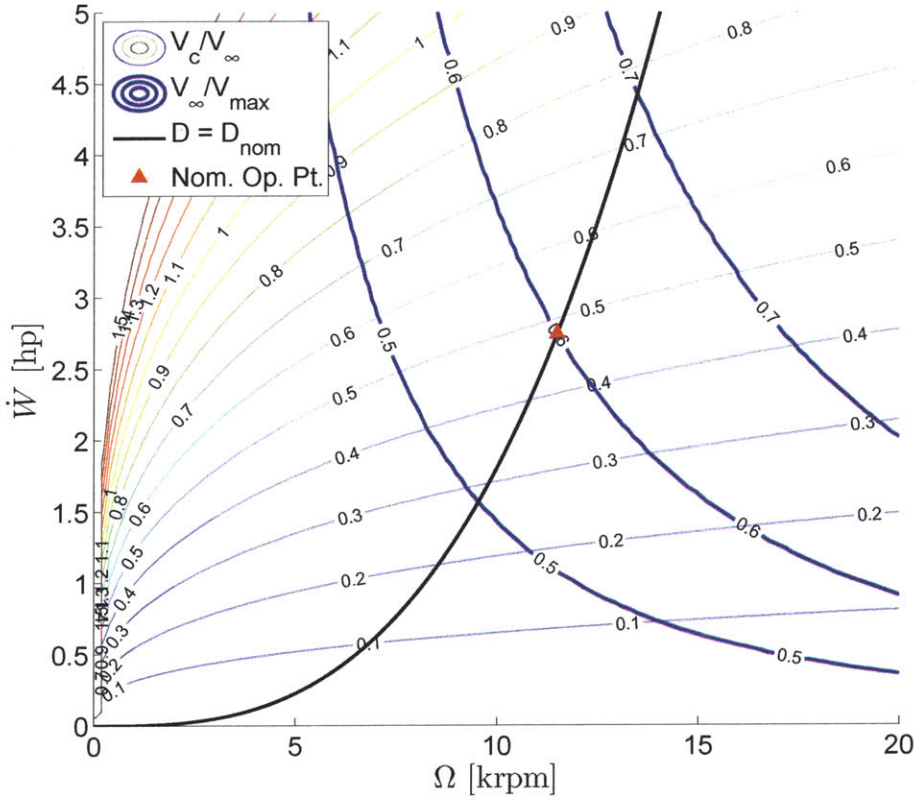

Figure 2-5: Minimum required cooling air velocity, V_c as a function of operating point, 1:11 scale.

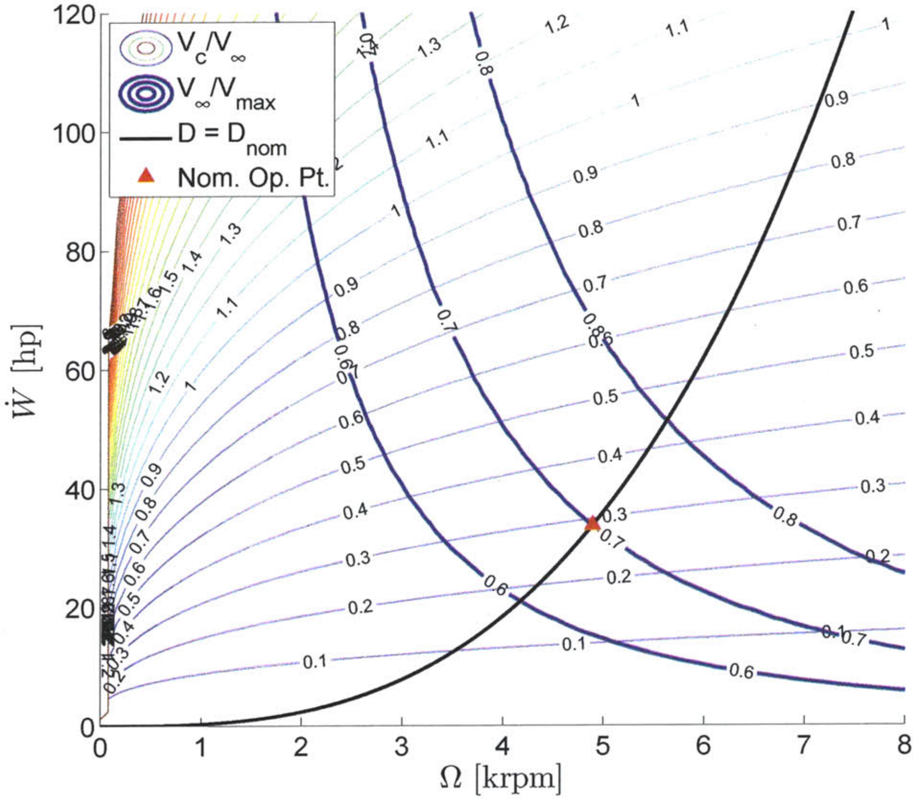

Figure 2-6: Minimum required cooling air velocity, V_c as a function of operating point, 1:4 scale.

2.4.2 Water Cooling

For water cooling, waterjackets can be purchased which consist of an aluminum cylinder slid over the motor casing and fitted with inlet/outlet pipe attachments. O-rings maintain the seal between the motor case and the aluminum jacket, allowing contact between cooling flow and motor skin.

The required water mass flow can be estimated from Eq. 2.30 as 1.2 gal/hr and 6.1 gal/hr for the 1:11 and 1:4 scale models, respectively. For water cooling pumping pressure must be provided to overcome losses in the long tubing lines because cooling tubes will run from outside the test section, up the mounting pylon, through the fuselage, into the propulsor and back out again. A conservative estimate for this total length is 200 ft. of tubing.

The required pumping pressure can be estimated from Colebrook's equation [18]

$$\frac{1}{\lambda^{1/2}} = -2\log\left(\frac{2.51}{Re\lambda^{1/2}} + \frac{e/D}{3.72},\right) \tag{2.32}$$

where ${}^{e}/_{D}$ is the relative pipe roughness and λ is the Darcy-Weisbach friction coefficient [18]. The head loss is

$$\Delta p = \frac{1}{2}\rho V^2 \lambda \left(\frac{l}{d_h}\right). \tag{2.33}$$

Water lines will be routed through a bifurcation structure in the propulsor flowpath from the fuselage, and into the motor cavity. To keep the bifurcation thin, it is desirable that cooling lines be no larger than 1/8 in. diameter for the 1:11 scale model. The pressure requirement is impractical (approximately 200 psi) if all 200 ft. of tubing are of the same small diameter, so we use a larger diameter tube (3/8 in.) to cover the majority of the distance, keeping the 1/8 in. line to roughly 20 ft. For the 1:11 scale case, this means the pressure drop is 21 psi per propulsor. For the 1:4 scale case, it is likely that a larger diameter 1/4 in. tube will fit through the propulsor bifurcation, and the line pressure drop will be only about 8 psi per propulsor.

2.5 Conclusions

Similar results are obtained for motor parameters whether we match the full-scale value of η_p or ${}^{C_x}/_{V_\infty}$. There are also no substantive benefits from changing the overall scale of either model because there are several commercial motors available with the size, power and speed to allow testing in the desired speed range at the LaRC 14'×22' wind tunnel. Of these the NeuMotors 1530 and HPEVS AC-50 seem the best choices. Waste heat may be removed from these motors using either core air flow or a water-cooling system. For air cooling, minimum core velocities are estimated to be around 30% and 50% of the freestream for the two models. If water cooling is selected there are only small mass flows of water needed, with the losses in the delivery lines amounting to about 21 psi for the 1:11 scale.

Chapter 3

Nacelle Aerodynamic Design and Optimization

In addition to specifying a suitable electric motor, we also need to design the propulsor which will house it. This process involves three key steps: aerodynamic design of the nacelle and centerbody, design of the rotor and stator, and structural design of the components. We consider here the aerodynamic design of the podded propulsor flowpath. Rotor and stator design is outside the scope of this thesis, and has been undertaken as a separate part of the N+3 project [9]. Structural design is treated in Chapter 4.

A goal of the experiments is to assess the benefit of boundary layer ingestion by comparing the performance of the podded and integrated test articles. To provide a fair comparison, losses on the podded configuration nacelle need to be representative of those on the full-scale aircraft, with the nacelle having an efficient aerodynamic design while operating at appropriate thrust and propulsive efficiency. This is a problem which lends itself to gradient-based optimization [11]. Application of such methods has the additional benefit of automating the design process. Nacelle performance is sensitive to changes in blading, target operating point, tunnel speed, electric motor size and model scale, and an automated design tool eases iteration of these parameters. A rapid design capability is of particular utility in the definition of the multiple centerbody trailing-edge plugs used to vary nozzle area and mass flow.

To apply optimization methods to this problem, we express the relevant design features as a finite set of variables which are iteratively updated during the optimization process. The design is discretized as shown in Fig. 3-1, which indicates the location of the optimizer degrees of freedom. The nacelle airfoil and centerbody are cubic B-splines [19] through the marked control points. There are eleven degrees of freedom in the control points, which have been chosen to allow the optimizer to create a wide range of airfoil and centerbody shapes. The rotor speed and nacelle chord length are also variable. The chord length scales the entire nacelle airfoil. The spinner and blading are fixed inputs to the design. The bifurcation airfoil is a symmetric NACA 0018 with a hollow central passage allowing power, cooling and instrumentation lines access to the motor cavity. Constant hub and shroud radii are maintained from the rotor trailing edge through the stator passage for ease of manufacture, as described in Chapter 4.

The formal optimization problem is

$$\min \mathcal{K}\left(\vec{X}\right) = \sum_{\text{wakes}} \frac{{}^{1}\!/_{2}\rho_e u_e^3 \theta^*}{\rho u^3 L_{ref}}, \tag{3.1}$$

$$\text{s.t.} \qquad \eta_p = \eta_{p,\ \text{spec}}\,, \tag{3.2}$$

$$C_T = C_{T,\ \text{spec}}\,. \tag{3.3}$$

The subscript e denotes boundary layer edge quantities, θ^* is the kinetic energy thickness of a given viscous wake, and $\mathcal{K}$ is the normalized net kinetic energy defect, summed across all the viscous wakes. Minimization of $\mathcal{K}$ is equivalent to minimizing the kinetic energy loss. $\eta_{p,\ \text{spec}}$ and $C_{T,\ \text{spec}}$ are the desired propulsive efficiency and thrust coefficient for the configuration being evaluated. The thrust target is a simulated cruise condition and the propulsive efficiency goal is as discussed in Chapter 2.

$\mathcal{K}$ is evaluated for each design vector $\vec{X}$ using the MTFLOW (Multi-passage ThroughFLOW) Design/Analysis Program, an axisymmetric interacting boundary layer theory (IBLT) solver written by Drela [20]. MTFLOW solves the axisymmetric Euler equations along an iteratively updated streamline grid, and allows the addition

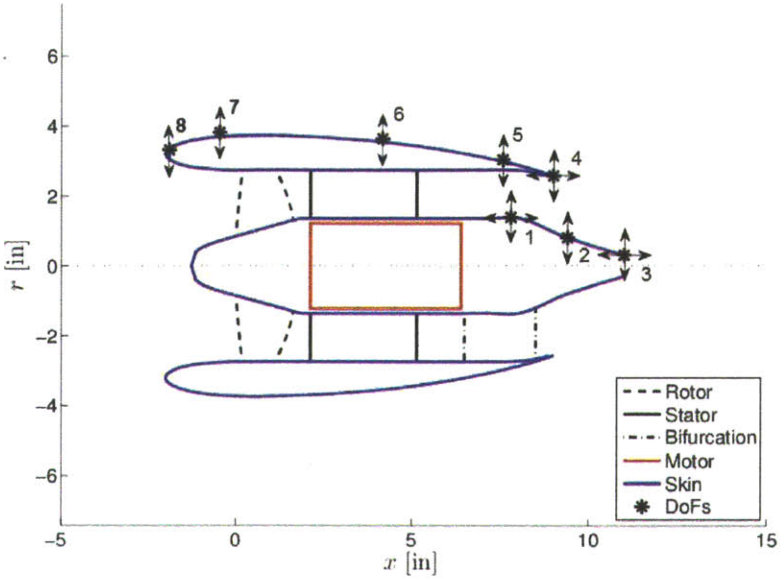

Figure 3-1: Optimizer degrees of freedom and control point numbering. Rotor speed and nacelle chord are also variable.

of swirl by blades of specified geometry and rotational speed. Losses on the blades are not captured. The integral boundary layer method matches flow quantities at the boundary layer edge. Transition is captured using an 'envelope e^N' method in which disturbance amplitudes are assumed to grow according to

$$||\mathbf{u}'||\,(x,\omega) = ||\mathbf{u}'||_0\, e^{N(x,\omega)}\,, \tag{3.4}$$

and the mode of most interest at any given x location is that which is growing most quickly, i. e. the one with the largest N value regardless of frequency [21]. The maximum N is approximated by the use of curve-fits developed from boundary layer profile families such as Falkner-Skan, and when N exceeds some critical limit N_{crit}, transition is assumed to occur. Because N is a disturbance growth factor, a larger specified N_{crit} value for transition corresponds to lower disturbance initial flow. For the MIT WBWT, $N_{crit} \approx 4$ is appropriate [21].

The optimizer function itself is the MATLAB `fmincon` function [22], a sequential quadratic programming (SQP) method. Gradient-based methods start by computing the n-dimensional gradient about a user-supplied start point via finite-differences. The optimizer then takes a step along the n-dimensional path of steepest slope. A true Newton method would compute the matrix of second derivatives at each optimizer point to determine the length of the step, but this is computationally expensive. `fmincon` makes use of a quasi-Newton method, in which the Hessian is not calculated explicitly, but is instead approximated based on previous function evaluations. As the optimizer runs the approximation to the Hessian is continuously updated and convergence approaches second-order [11].

3.1 Design of Experiments

A key failing of gradient-based methods is the risk of the algorithm becoming trapped in a local optimum, without the ability to detect adjacent optima. Gradient-based methods are thus best applied to convex design spaces, in which only a single optimum exists. There is no such guarantee for the design space of interest and it is imperative to explore broadly before relying upon the results of any particular optimization. This can be accomplished in a number of ways, through the use of multiple start points, heuristic algorithms, or design of experiments (DoE).

DoE is a structured method of design space exploration making use of orthogonal arrays [11]. Orthogonal arrays are combinatorial design constructs which for a particular number of variable values represent a balanced subset of the full-factorial experiment. In an orthogonal array of constant strength, as we will consider here, each possible combination of variable values occurs and all occur an equal number of times. The simple example shown in Table. 3.1 is known as an $L_4\left(2^3\right)$ array, because four experiments are required, exploring three variables at two possible levels.

These formulations maintain orthogonality between the various factors, and allow variable main effects to be extracted by comparing the average function value when each variable is at a particular setting to the average over the entire experiment. These main effects can be used to inform the choice of start point for the gradient-based optimizer. For our thirteen variable design space, DoE is performed using an

Expt.	Variable		
No.	A	B	C
1	A1	B1	C1
2	A1	B2	C2
3	A2	B1	C2
4	A2	B2	C1

Table 3.1: $L_4\left(2^3\right)$ orthogonal array.

$L_{27}\left(3^{13}\right)$ array to explore each variable over three possible levels. The computed main effects on the net kinetic energy defect $\mathcal{K}$ of each variable setting are shown in Fig. 3-2, where settings 1, 2 and 3 correspond to minimum, middle and maximum values, respectively.

As the goal is to minimize $\mathcal{K}$, negative effects in Fig. 3-2 are desirable. Perhaps the most easily understood of the main effects is that of airfoil chord, c. Fig. 3-2(c) shows that loss is minimized when c is at its shortest, as expected. Similar insight can be gained into each of the variables from the main effects presented in Fig. 3-2, and a configuration is suggested which is used as the initial guess for the gradient-based optimizer.

The proposed design has a thin airfoil of the minimum chord to encompass the entire bifurcation (seen on Fig. 3-1), and a tapered centerbody trailing edge. This design has a $\mathcal{K}$ value of 1.07×10^{-3}, which outperforms all designs investigated as part of the DoE (average $\bar{\mathcal{K}} = 1.46 \times 10^{-3}$). Interaction effects between variables are not captured by the DoE, and are left to the optimization routine. The performance of the DoE as described does not provide a guarantee that the optimum found via gradient-based optimization will be global, and we rely on the use of multiple start points to ensure that the minimum obtained is the best available in the design space.

3.2 Optimization

From the start point defined in Sec. 3.1 we can proceed to gradient-based optimization to refine the nacelle and centerbody design. The results of the optimization are given

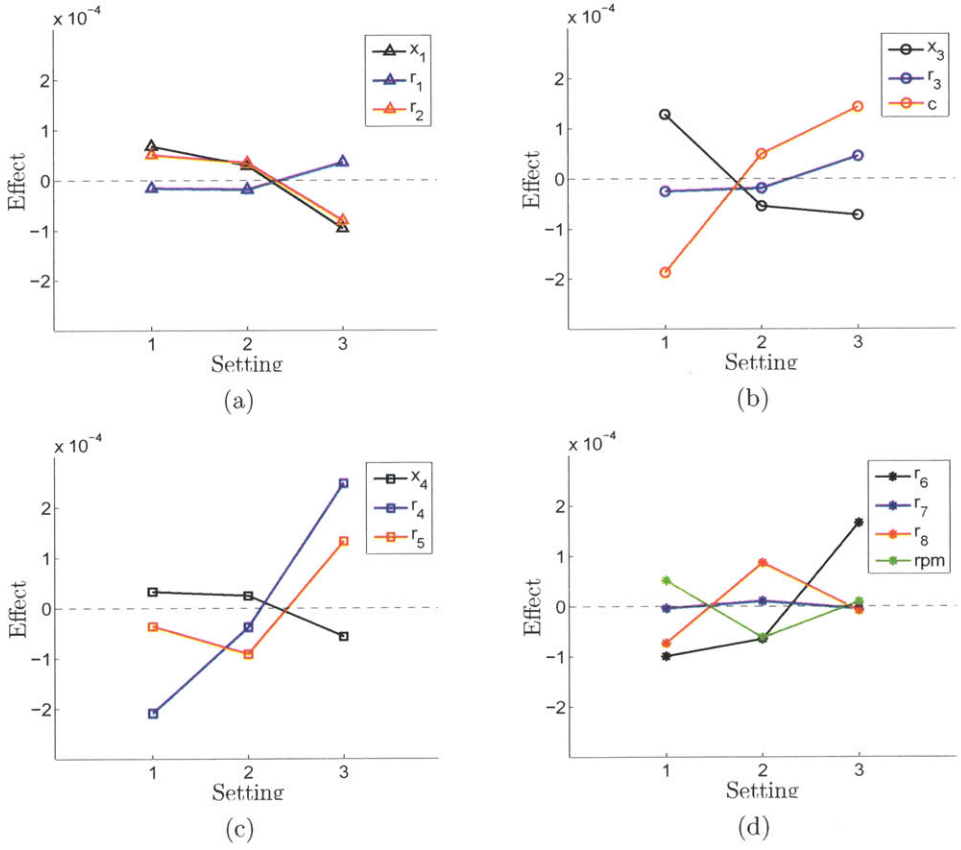

(a) (b) (c) (d)

Figure 3-2: Design variable main effects. Settings 1, 2 and 3 are respectively the minimum, middle and maximum values examined for each variable. See Fig. 3-1 for control point numbering.

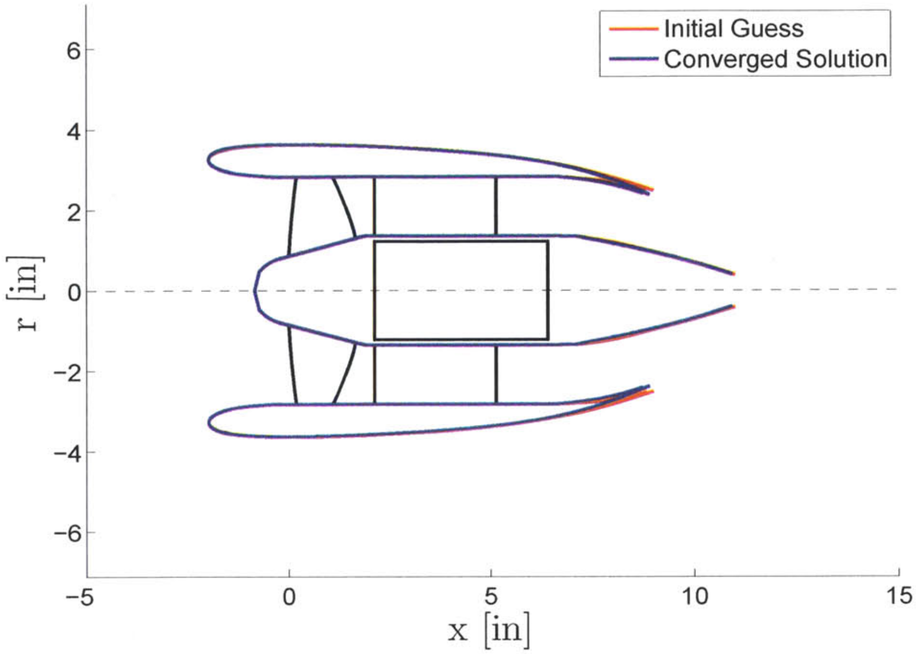

Figure 3-3: Optimizer geometry changes. Additionally, motor speed is reduced from 14.90 to 14.77 krpm.

in Fig. 3-3, in which the net kinetic energy defect is reduced to $\mathcal{K} = 9.27 \times 10^{-4}$, an improvement of 13.4%. The small scale of the changes shown in Fig. 3-3 is a testament to the utility of the DoE.

Contours of Mach number overlaid by streamlines for the optimized design are given in Fig. 3-4. The separation region at the centerbody trailing edge (shown as white) represents one of the key optimizer trades. A blunt centerbody trailing edge is more efficient than a sharp trailing edge because of the residual swirl in the flow downstream of the stator. The swirl is shown in Fig 3-5, which gives contours of V_θ/V_∞. The stator is designed to remove all swirl but it is difficult to avoid some small amount, resulting in an axial vortex downstream of the stator trailing edge. If flow remains attached along the trailing edge of the centerbody, the radius of the innermost streamtubes containing this swirl approaches zero with consequent high tangential velocities. These high velocities result in increased kinetic energy in the wake and decreased vortex core pressure giving a pressure drag on the propulsor.

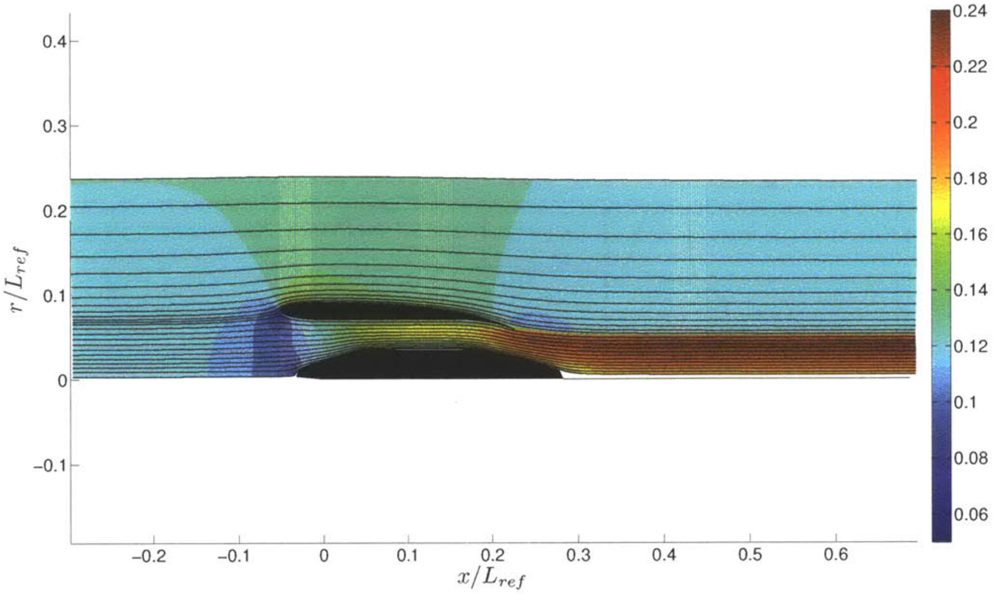

Figure 3-4: Optimized flowpath design: contours of Mach number with streamlines overlaid.

Having the boundary layer separate at a larger radius mitigates these effects. The most efficient design is therefore obtained by balancing the weakening of this vortex against the entropy generation associated with boundary layer separation from a blunt trailing edge. This balance governs the design of the centerbody trailing edge.

There are also constraints we impose on the optimizer. The propulsors are intended for low-speed tests, and the optimization is carried out at Reynolds numbers of approximately 3×10^6 ($V_\infty = 100$ mph) where it becomes possible to design an airfoil with substantial laminar flow. The optimizer attempts this by pushing the start of the adverse pressure gradient on the rear of the airfoil downstream. The adverse pressure gradient causes a laminar separation bubble which triggers boundary layer transition and subsequent re-attachment. Delaying or weakening the adverse pressure gradient moves transition downstream, resulting in a thick and highly curved airfoil suction side, with transition as far downstream as the 50% chord. Such a nacelle has low drag compared to one designed for operation at full-scale in which transition is expected at or before 15% chord [23]. This affects the comparison between the

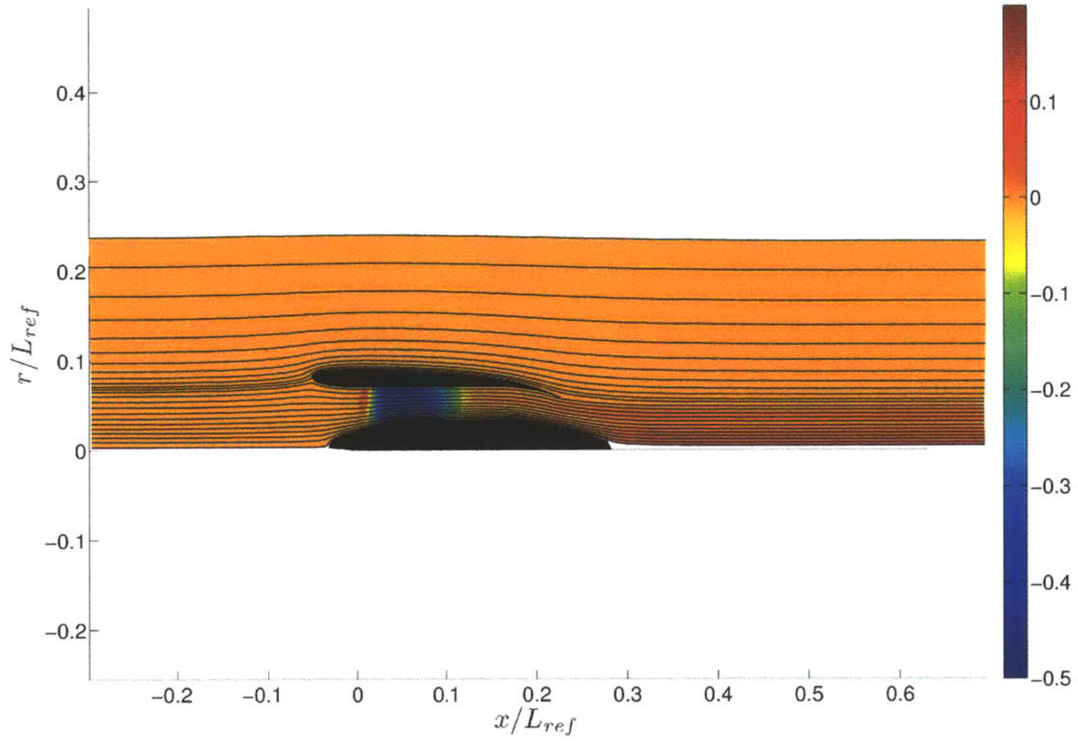

Figure 3-5: Optimized flowpath design: contours of V_θ/V_∞.

integrated and podded D8 configurations because a secondary effect associated with the BLI configuration is the reduction in nacelle wetted area and pylon drag because the lower half of the nacelle is integrated into the fuselage. Allowing the optimizer to maintain laminar flow on the nacelle reduces the measured BLI benefit in a way that is not representative of the actual aircraft.

It is thus necessary to control the onset of turbulent flow using a specified transition location in the computational model (and trip tape on the experimental model). The effect of specifying early transition at the 15% chord on the optimal airfoil design is shown in Fig. 3-6. The emphasis is on reducing the nacelle surface area by thinning and flattening the airfoil rather than maintaining laminar flow.

Losses from the nacelle outer surface are greater than those for either the inner nacelle or centerbody. Fig. 3-7(a) shows $\kappa(x)$, the normalized kinetic energy defect for each wake as a function of axial position,

$$\kappa(x) = \frac{{}^1\!/_2\,\rho_e u_e^3 \theta^*}{\rho u^3 L_{ref}}\,. \tag{3.5}$$

The loss behavior in Fig. 3-7(a) occurs in part because the wetted area of the nacelle outer surface is larger than the other surfaces. The surface pressure coefficients given in Fig. 3-7(b) for all three surfaces of the optimized propulsor show that the nacelle minimum pressure location is pushed well forward toward the leading edge. This leading edge pressure spike is optimal at zero-angle of attack, but reduces the angle of attack at which stall occurs. Effects of angle of attack cannot be captured by MTFLOW, which is axisymmetric. If α sweeps are to be performed with this nacelle installed, it may therefore be beneficial to examine stall margin using 3D CFD.

Another trade made by the optimizer governs the interplay between nozzle area, propulsive efficiency, thrust and rotor speed. Higher efficiency means a lower V_j, and thus a larger nozzle area for a given thrust, with effects on the nacelle inner trailing edge and centerbody shape at the nozzle (as in actual gas turbine engines) [8].

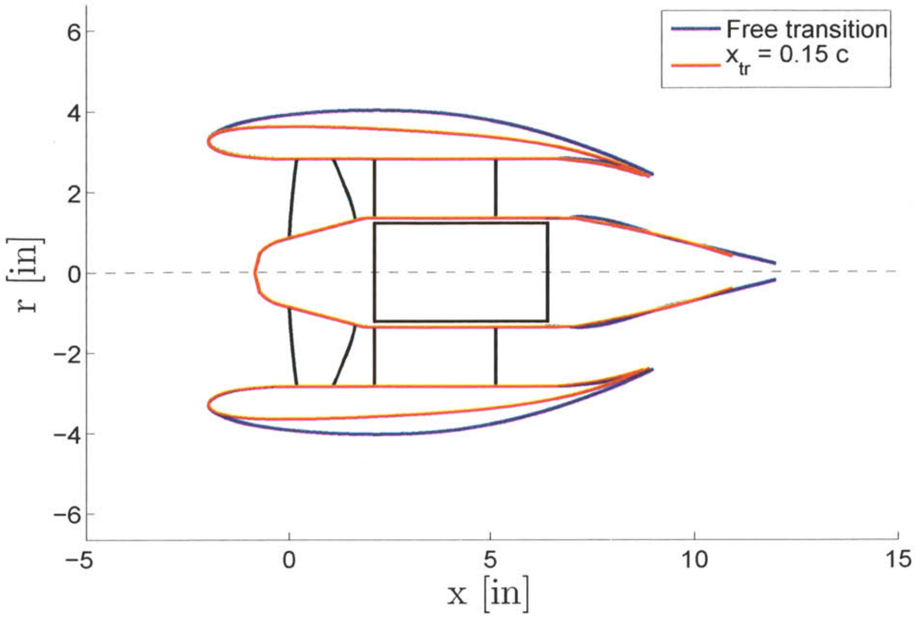

Figure 3-6: Optimal designs with free transition ($N_{crit} = 4$) and transition location specified at 15% chord.

3.3 Plug Definition

In both the COTS and custom propulsor designs, removable centerbody trailing edge plugs are used to change nozzle area to control mass flow. Centerbody plugs were chosen rather than variable nacelles for ease of replacement during testing. At least three nozzle plugs are desired for both propulsors, to allow operation at a range of mass flows bracketing the simulated cruise design point. There is some uncertainty in defining the geometry for the cruise condition because of a lack of precise information about the total airframe drag. As a result, for the COTS propulsor, nine plugs of varying size were designed and manufactured for the NASA wind tunnel tests. The plugs were designed using a modified version of the propulsor optimizer described above, in which degrees of freedom were allowed only along the centerbody trailing edge. A schematic of the four plug degrees of freedom is shown in Fig. 3-8.

The structural design of the COTS centerbody consists of a straight composite

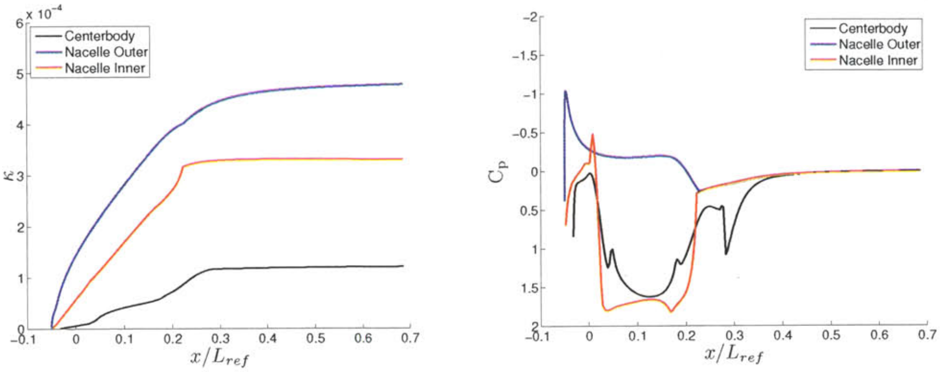

(a) (b)

Figure 3-7: Optimized nacelle design: a) normalized kinetic energy defect as a function of axial position for each wake; b) surface pressure coefficients.

stator section, followed by a metal adaptor ring which increases in radius from the stator trailing edge to a fixed point at the leading edge of the plug. The plugs are manufactured using a 3D-printing process known as fused deposition modeling (FDM). They slide over an aluminum inner cone which supports the plug and guides internal cooling flow over the motor and out an exhaust hole at the trailing edge. The inner cone also interfaces with the bifurcation downstream of the stator. The plugs are constrained to meet the adaptor ring at their leading edge and match its slope, as well as meet the inner plug at the trailing edge.

An FDM plug of the minimum possible size, shown in Fig. 3-8, was used in initial testing [9]. Due to the constraint on FDM minimum thickness, smaller trailing edge plugs are not feasible. Larger plugs can be designed by modifying the optimizer to hit a target mass flow, $\dot{m}$, as

$$\min \mathcal{K}\left(\vec{X}\right) = \sum_{\text{wakes}} \frac{{}^{1}\!/_{2}\rho_e u_e^3 \theta^*}{\rho u^3 L_{ref}}, \tag{3.6}$$

$$\text{s.t.} \qquad \dot{m} = \dot{m}_{\text{spec}}\,. \tag{3.7}$$

Four optimized plug geometries are illustrated in Fig. 3-9. Four additional plugs were defined by piecewise linear interpolation of the control points between the opti-

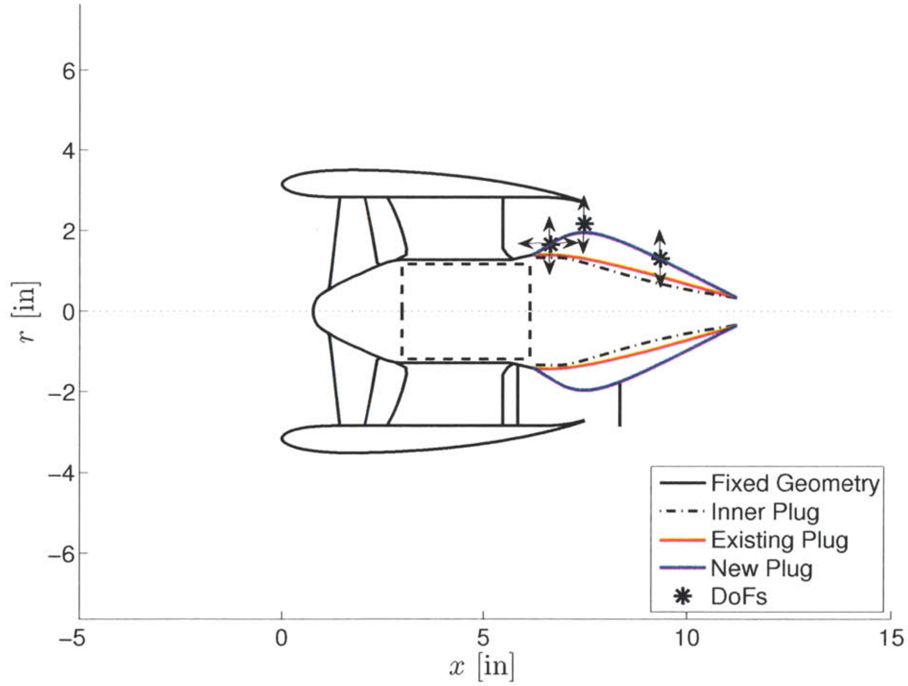

Figure 3-8: Four COTS plug degrees of freedom. Both position and slope are constrained at the plug leading edge, as is the trailing edge position.

mized designs. The plugs are numbered in order of increasing size, with plug #1 the existing one. Streamlines are shown for the smallest (#3) and largest (#9) optimized plugs in Figs. 3-10 through 3-11.

Two effects are worth noting for the largest plug. The most prominent is the separation area upstream of the plug leading edge in the vicinity of the stator. This is unavoidable given the existing geometric constraints if this low a mass flow is required because there is not enough axial room for a non-separated hub rise between the stator and the nacelle trailing edge. However, the kinetic energy information in Fig. 3-12 shows that the loss penalty of this separation area is small. The separation bubble is visible in the boundary layer shape parameter plot of Fig. 3-12 where $H > 4$. The centerbody kinetic energy defect remains at less than 10% of its downstream value through this region, because $\kappa \propto u_e^3$, and the edge velocity u_e in the vicinity of this separation bubble is less than half its value in the nozzle (see Fig. 3-11). Losses through the nozzle and over the plug trailing edge dominate $\mathcal{K}$ because of the high edge velocities in the jet.

Figs. 3-13 and 3-14 show that the separation affects the stator performance. Swirl velocities in the jet are approximately twice as high with the larger plug. The upstream separation region is severe for the largest two plugs. Its magnitude is reduced for plug #7 as in Fig. 3-15, with the separation area diminishing with shrinking plug size.

From comparison of Figs. 3-10 and 3-11 we can see a change in capture area. Plug #9 passes approximately 40% lower mass flow than plug #1, resulting in a 40% reduction in the upstream capture area and a change in the location of the stagnation point on the nacelle leading edge. There is thus a higher angle of attack on the airfoil and a change in the surface pressure distributions. The pressure distributions in Fig. 3-16 indicate that the larger plug sharpens the leading edge pressure spike on the nacelle outer surface and brings the airfoil closer to leading edge separation; the outer nacelle boundary layer shape parameter plot in Fig. 3-12 shows that $H \to 4$ near the leading edge. In the axisymmetric case with the aircraft α equal to zero the flow does not separate, but at higher model α there could be leading edge separation

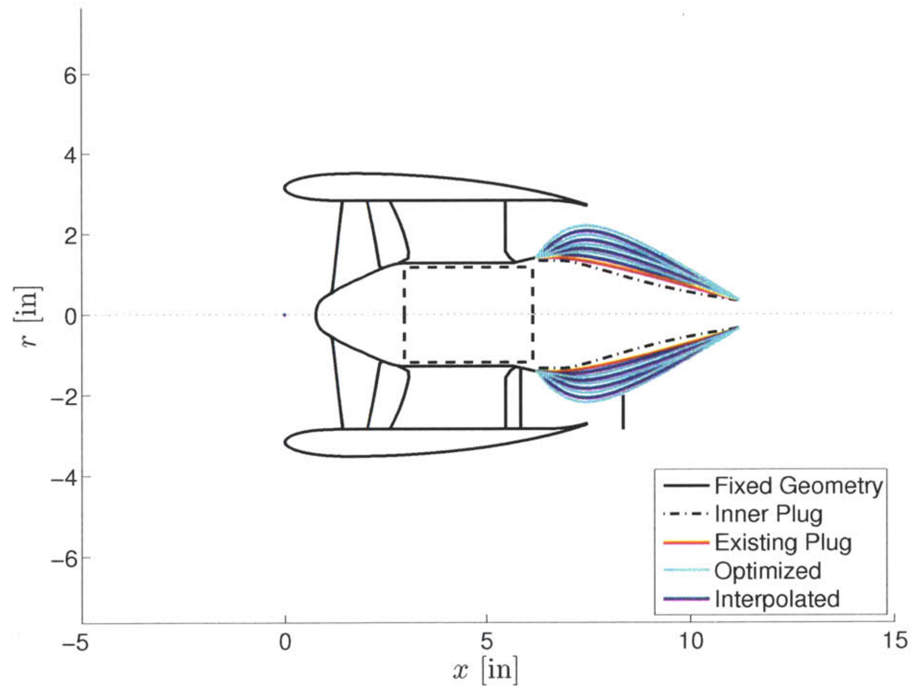

Figure 3-9: COTS plug geometries.

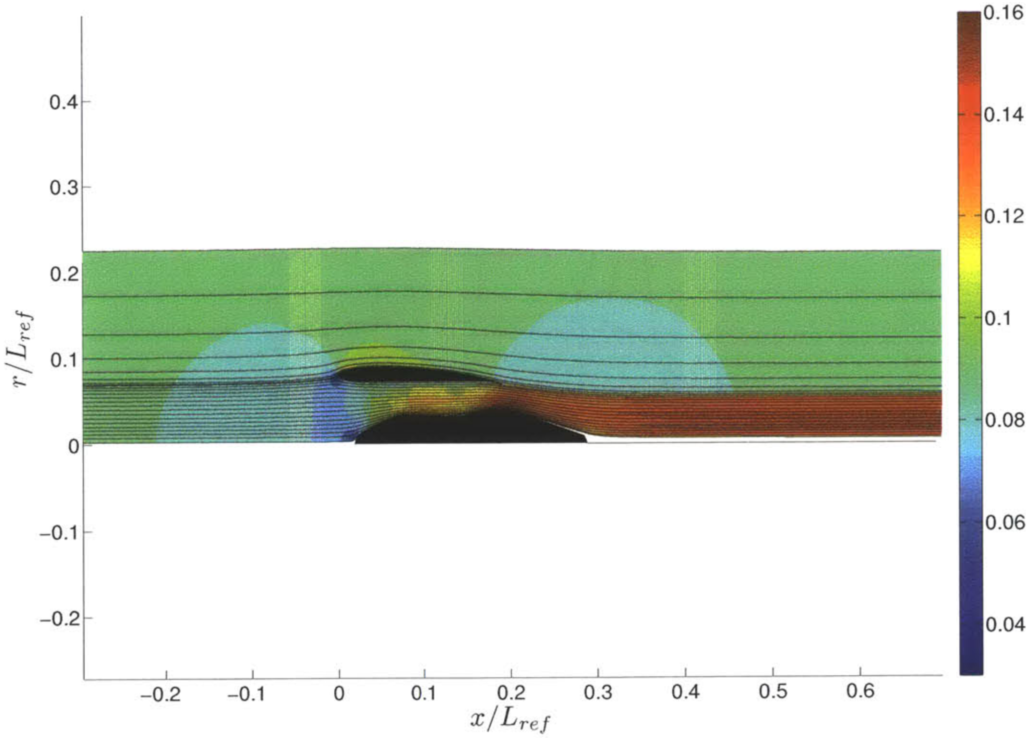

Figure 3-10: Smallest optimized plug (plug #3): contours of Mach number with streamlines overlaid.

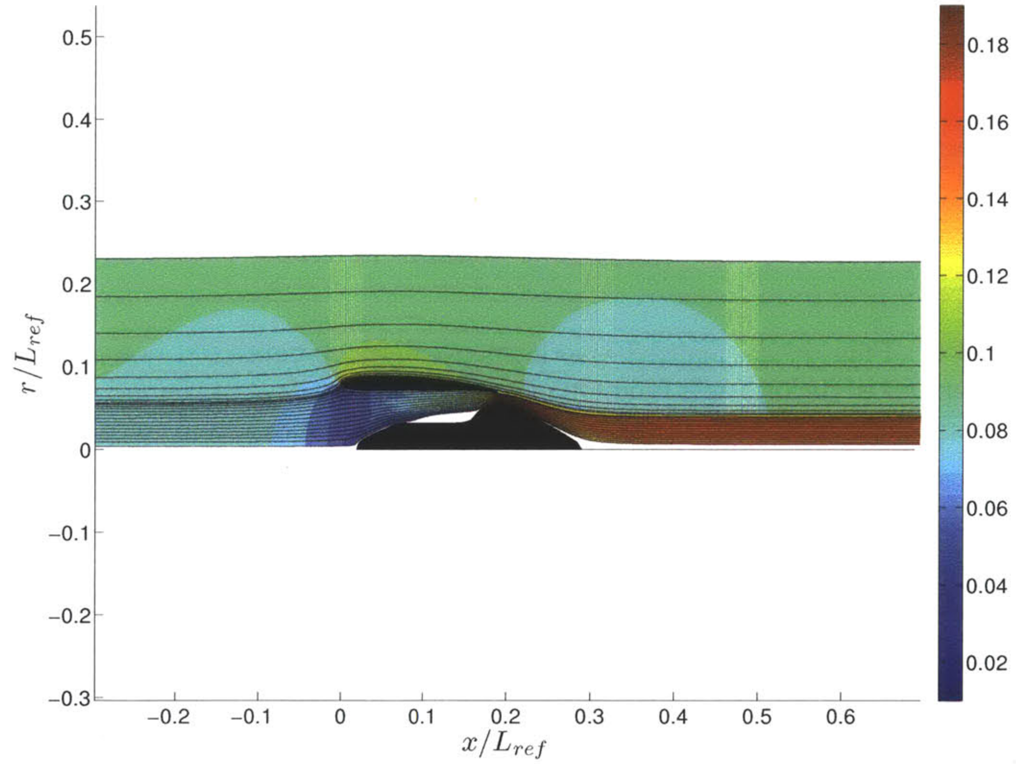

Figure 3-11: Largest optimized plug (plug #9): contours of Mach number with streamlines overlaid.

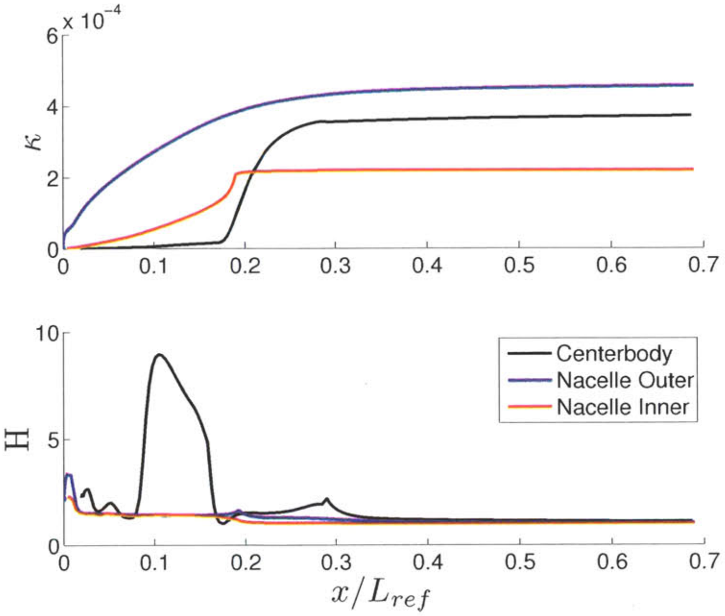

Figure 3-12: Plug #9 normalized kinetic energy defect (above) and boundary layer shape parameter (below) as a function of axial location.

on the nacelle when operated with the larger plugs.

3.4 Conclusions

An optimization tool has been developed for the design of the custom propulsor nacelle and centerbody. The tool, which allows rapid iteration of turbomachinery design, wind tunnel test point, and other relevant parameters, was used to find a performance improvement relative to the baseline design. The tool was also used for design of the COTS centerbody trailing edge plugs. Eight new COTS plugs were designed, allowing up to 40% reduction in mass flow. With the largest of these plugs, there is a risk of separation near the stator and nacelle leading edges and care must be taken to account for these effects if it becomes necessary to use these plugs. A similar exercise can be carried out using these tools to design additional plugs for the custom propulsor if necessary.

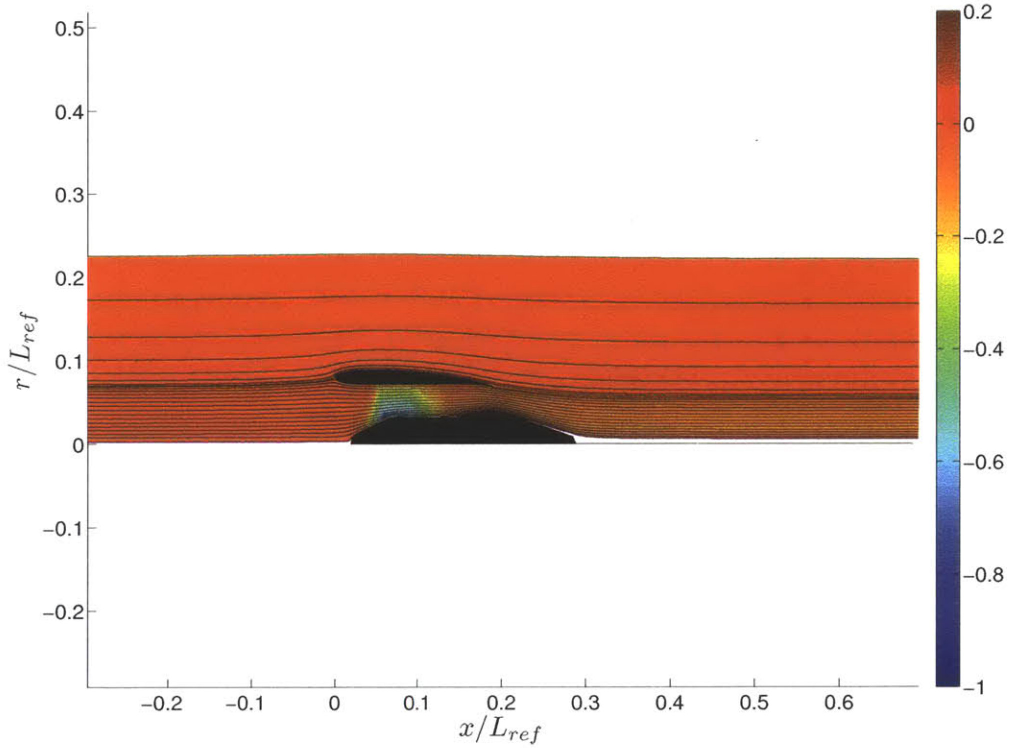

Figure 3-13: Plug #3: contours of V_θ/V_∞.

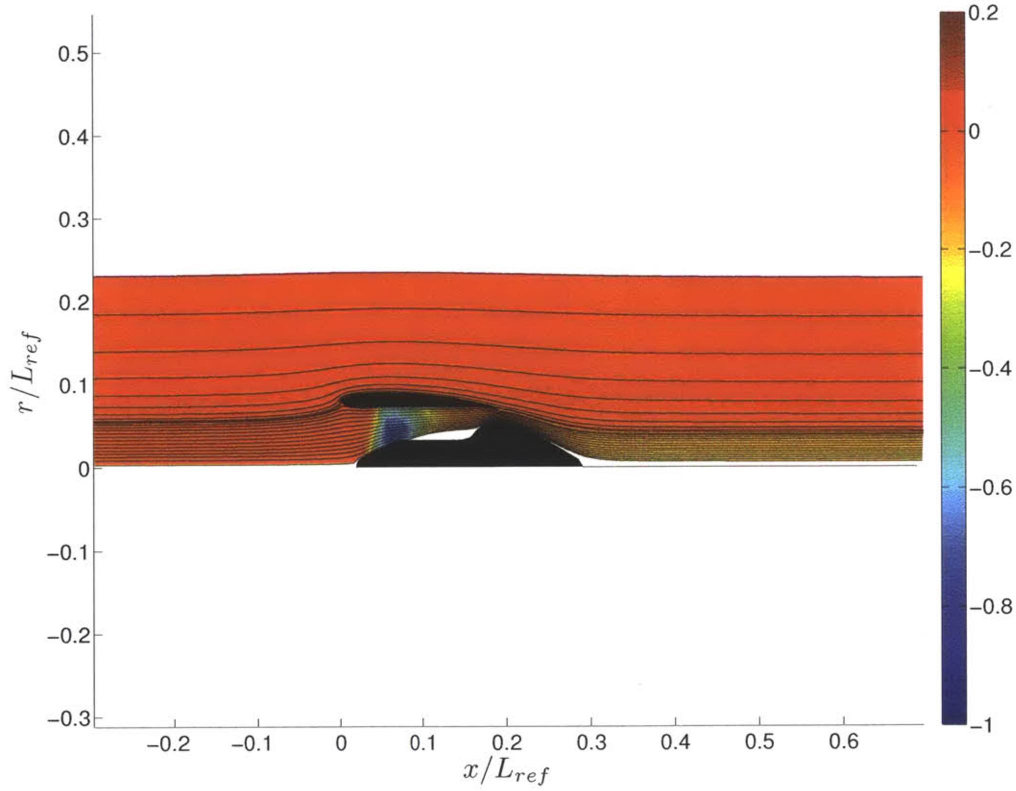

Figure 3-14: Plug #9: contours of V_θ/V_∞.

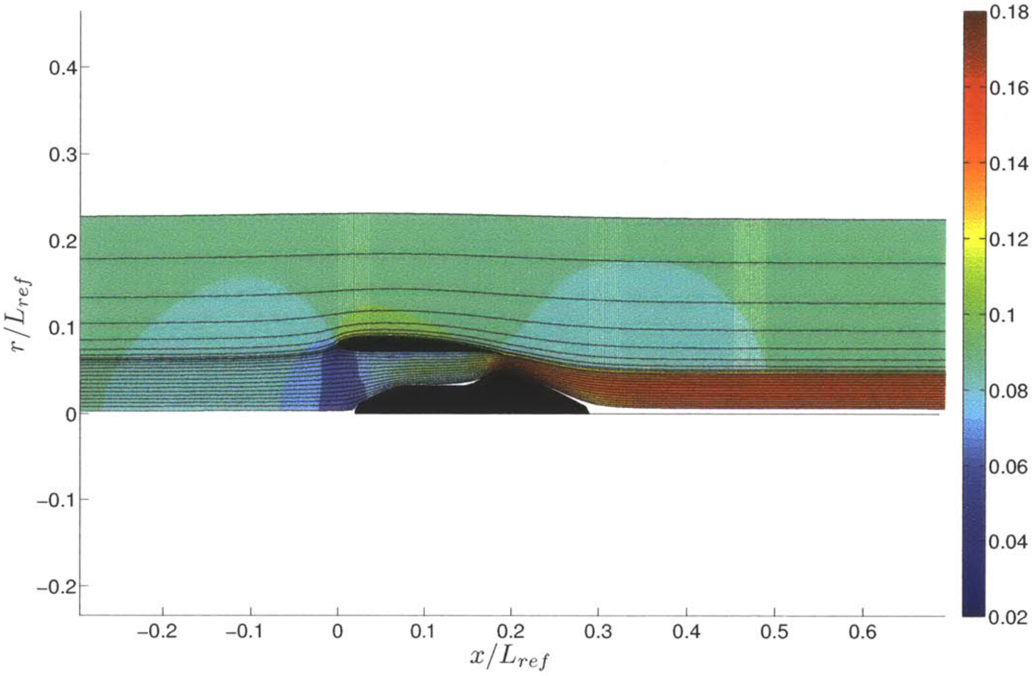

Figure 3-15: Plug #7: contours of Mach number with streamlines overlaid.

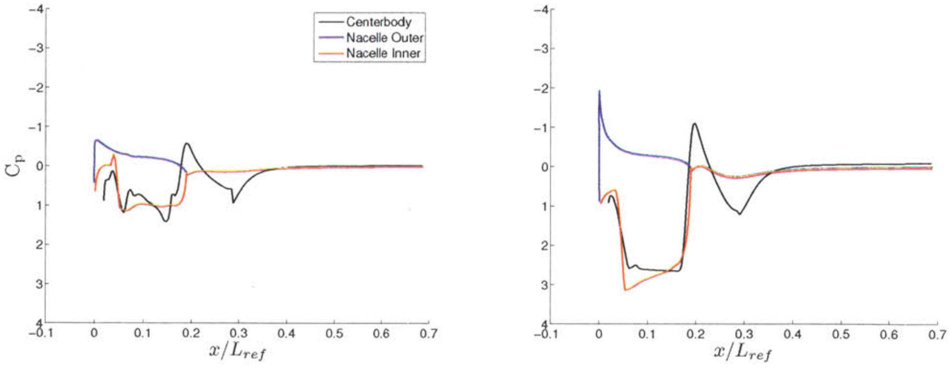

(a)

(b)

Figure 3-16: Surface pressure coefficient: a) plug #3; b) plug #9.

Chapter 4

Propulsor Mechanical Design

The third part of the design included in this thesis is the mechanical design for manufacture and assembly of the 1:11 scale podded custom propulsors. While the design is informed by the layout of the existing 1:11 scale COTS propulsors, there are differences because of the use of water cooling and of custom machined aluminum turbomachinery, rather than air cooling and off-the-shelf carbon fiber blading. Improvements include easing centerbody plug replacement, motor cavity access and installation of static pressure taps.

The design presented here has passed a preliminary design review, but is not yet in final form. Iteration is required before parts are ordered to update the turbomachinery blading, size fasteners and fillets and to check that all factors of safety are in line with NASA LaRC requirements. Some other small modifications are also suggested as noted below. Where possible, parts are designed to be 3D printed using FDM. Structural members and those requiring small features, such as sharp trailing edges, are machined from aluminum.

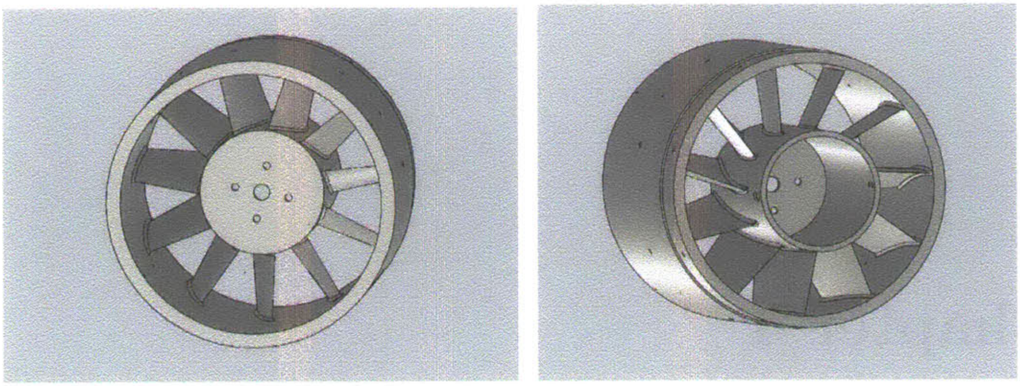

(a) (b)

Figure 4-1: Machined aluminum shrouded stator: a) view from upstream; b) view from downstream.

4.1 Physical Layout

4.1.1 Shrouded Stator and Electric Motor Installation

The primary structural component of the propulsor is an 11-blade shrouded stator section, machined in a single piece from aluminum as shown in Fig. 4-1. Initial discussions with TURBOCAM International [24] indicate that such a part can be manufactured on a computer numeric control (CNC) mill by machining axially from the upstream direction, then turning the part and machining from the rear, provided that the hub and shroud radii are constant. The stator has a faceplate on the upstream end of the hub containing a number of holes. These allow the electric motor to be mounted inside the hub using four M4 machine screws as shown in Fig. 4-2(b). The motor is cantilevered from the front, with water cooling, power and instrumentation lines running axially out the back of the stator hub. Holes and notches in the stator shroud are designed to interface with other parts.

4.1.2 Nacelle Trailing Edges and Pylon

To achieve a sharp trailing edge, it is necessary to machine the rear sections of the nacelle rather than using 3D printing. There are two trailing edge pieces which bolt

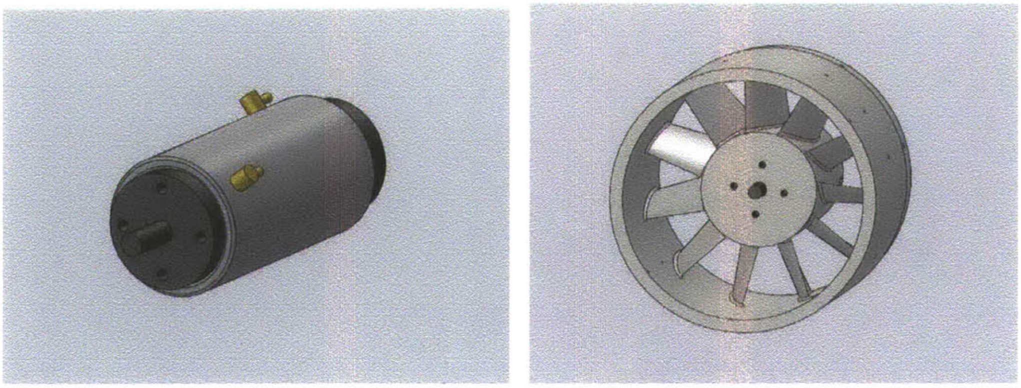

(a) (b)

Figure 4-2: Electric motor installation: a) motor with installed water jacket; b) installed inside stator hub cavity.

onto the downstream end of the stator section as in Fig. 4-3. Steps are machined in all three pieces to ensure axial alignment. The lower trailing edge section has a notch in its outer surface which interfaces with the pylon connecting the propulsor to the aircraft fuselage.

The pylon consists of leading edge and trailing edge parts as in Fig. 4-4. The leading edge is load-bearing and machined from steel. It has a hole drilled through its spanwise extent which is used to pass lines from the static pressure taps installed in the nacelle. This hole must be drilled using a long bit from both ends to meet in the middle (in the same manner which was used to manufacture the pylon in the COTS propulsor). The routing of the pressure lines will be discussed more fully in Section 4.1.5.

The pylon trailing edge is hollow. Power, cooling and instrumentation lines will be passed through this channel from the fuselage to the motor cavity. Together, the pieces form an symmetric airfoil. The countersunk attachment holes seen in Fig. 4-4(a) can be filled with clay (or taped) during testing so as to minimize disturbance of the flow. The same is true of all fastener holes which are exposed to airflow.

The steel pylon leading edge bolts to the aluminum lower nacelle trailing edge. There is an airfoil-shaped hole in the nacelle which allows passage of the lines inside the pylon. Near the leading edge of this hole on the inner nacelle surface is a notch

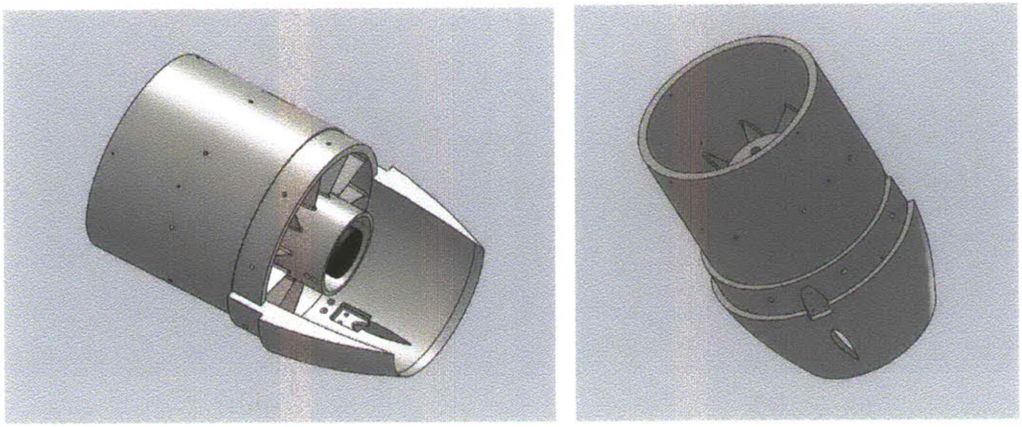
(a) (b)

Figure 4-3: Lower nacelle trailing edge: a) view from above; b) view from the direction of the fuselage.

and tapped holes which are used to align and attach a bifurcation which is discussed below. The nacelle trailing edge is completed by an upper section which is similar to the lower section, but without the various notches and holes for the pylon and bifurcation. This can be seen along with the installed pylon in Fig. 4-5.

4.1.3 Bifurcation and Centerbody Trailing Edge Plug

A hollow bifurcation downstream of the stator allows power, cooling and instrumentation lines to run into the motor cavity. The lines necessary to pass through this bifurcation are shown in Fig. 4-6. The bifurcation itself is a symmetric NACA 0018 airfoil. In the current version of the mechanical design, the bifurcation leans along its radial extent to sit directly in the wake of a stator blade as in the COTS propulsor. It has since been decided that this is unnecessary and the bifurcation could run vertically. The bifurcation is 3D printed in a single piece which interfaces with the nacelle trailing edge and stator hub as in Fig. 4-7(a). The tabs extending into the hub and nacelle ensure alignment, but also require that the bifurcation be installed in the lower nacelle trailing edge before either piece is attached to the stator. The bifurcation is open at rear to allow the motor to be extracted without removing the bifurcation.

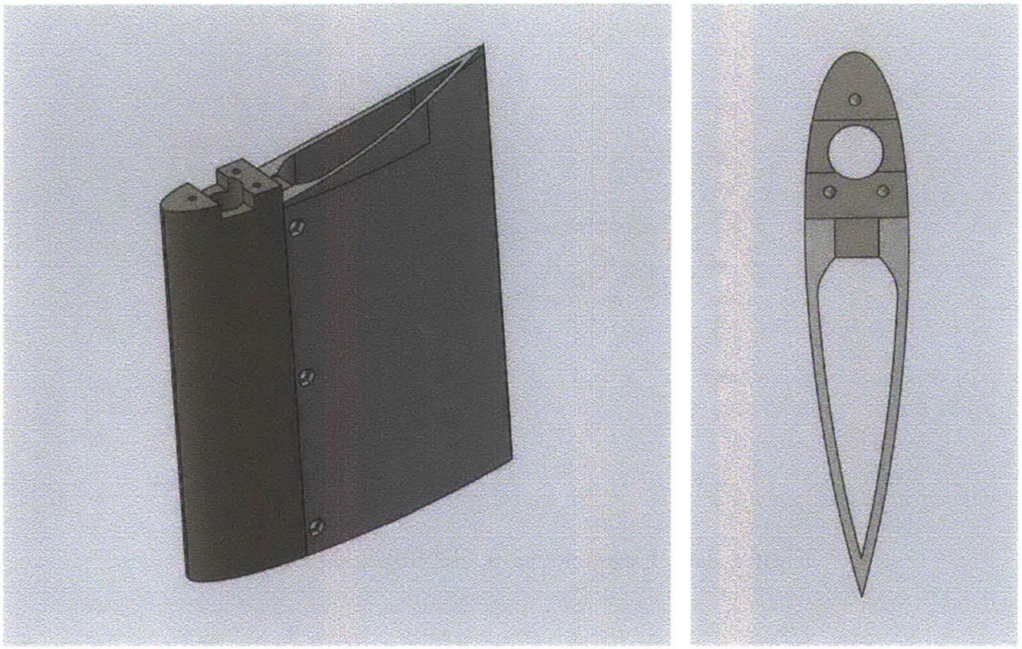

(a) (b)

Figure 4-4: Pylon connecting propulsor to fuselage: a) view from side. Hollow aluminum trailing edge bolts to steel leading edge; b) view from top.

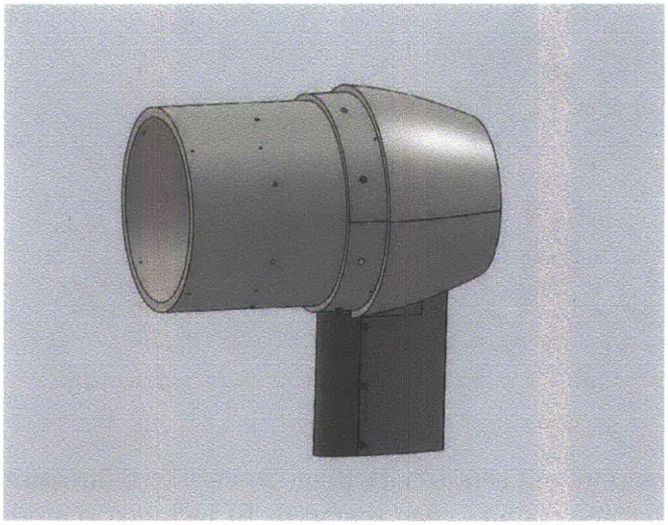

Figure 4-5: Stator, nacelle trailing edges and pylon attachment to fuselage.

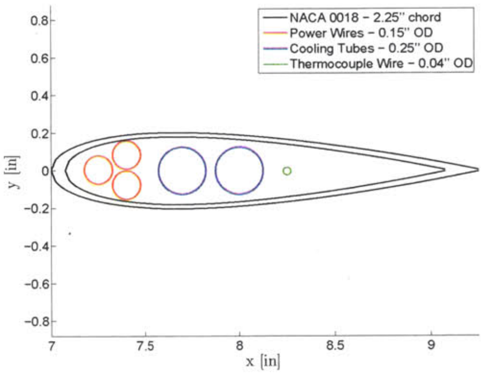

Figure 4-6: Cross section of bifurcation airfoil.

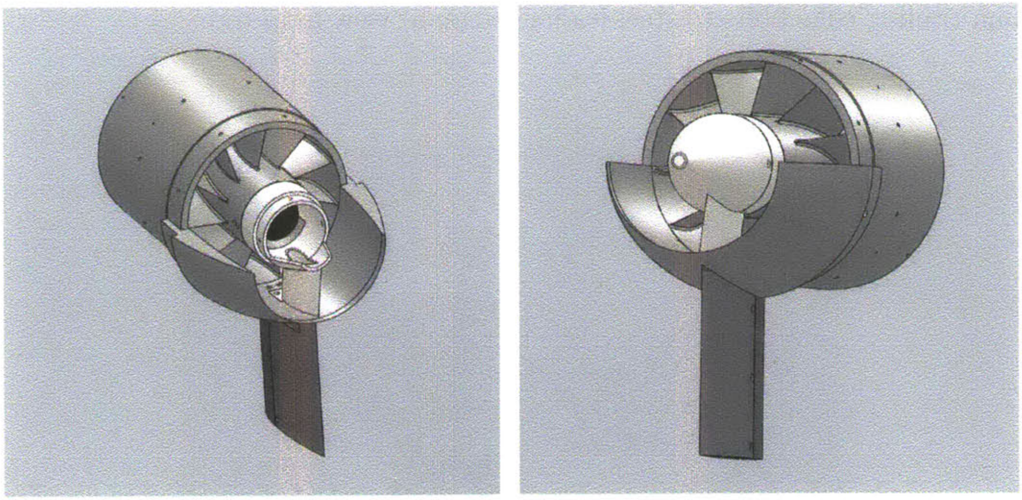

(a)

(b)

Figure 4-7: Bifurcation and centerbody plug: a) view of bifurcation from above with plug and upper nacelle trailing edge removed; b) installed centerbody trailing edge plug.

As in the COTS propulsor, removable FDM centerbody trailing edge plugs of varying size are used to control mass flow. Multiple plugs will be used during testing, and easy removal of these plugs is desirable. In the proposed custom propulsor design, the plug leading edge is just downstream of the maximum thickness of the bifurcation airfoil, which allows the plugs to slide onto the bifurcation piece from downstream. They are fastened to the bifurcation using three countersunk hex-key bolts. It will be possible to reach these bolts from the rear using an Allen key and change plugs without removing any other pieces of the nacelle.

The design of this trailing edge centerbody section is substantially different from that used in the COTS propulsor, in which plugs are 3D printed in one part with their own bifurcation. This necessitates removal of many propulsor parts to change the plug or remove the motor. It should be noted that these alterations are simplified by the use of water- rather than air-cooling for the electric motors as no provisions must be made for core flow.

4.1.4 Rotor Attachment

Like the stator, the rotor shown in Fig. 4-8(a) is CNC machined from a single piece of aluminum. As drawn, it attaches to the motor shaft using a commercially available collet-type propeller adaptor of the sort commonly used in RC aircraft. The adaptor can be seen installed in the proposed configuration in Fig. 4-8(b). A nose cap with a threaded tab may be used to complete the contour of the hub spinner as shown in Fig. 4-9. This fairing screws into the rotor hub leading edge, whose inner surface is threaded, and can be tightened using a rod through the radial holes in the nose cap. This part may be 3D printed using FDM, or machined from a harder plastic such as Delrin to provide for longer-life threading.

The propeller adaptor consists of the four pieces shown in Fig. 4-10. There is a threaded rod with a collet on one end, a housing through which the threaded rod is drawn, a washer and a steel hex nut. The housing internal surface tapers such that tightening the nut on the rod draws the collet back into the housing and tightens it over the motor shaft. The washer and flat surface of the housing are roughened to

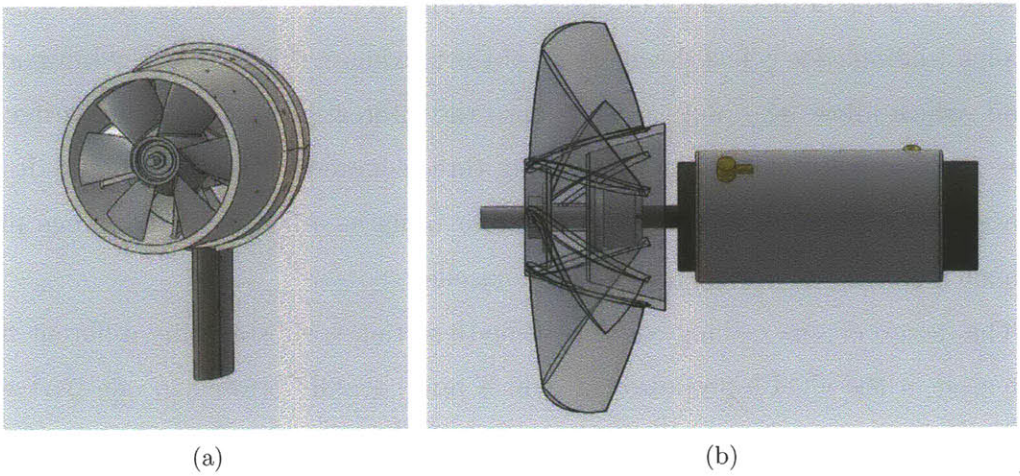

(a) (b)

Figure 4-8: Rotor attachment: a) installed in propulsor; b) attached to motor shaft using collet-type propeller adaptor.

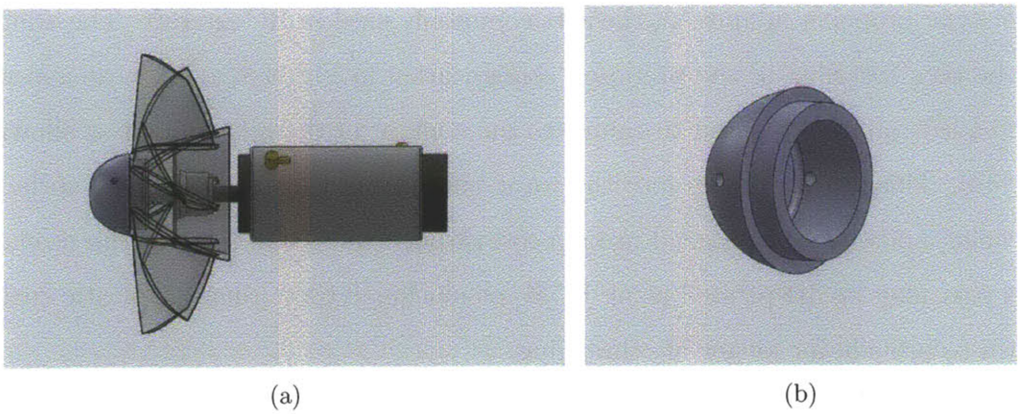

(a) (b)

Figure 4-9: Nose cap: a) installed in rotor; b) isolated view from the rear.

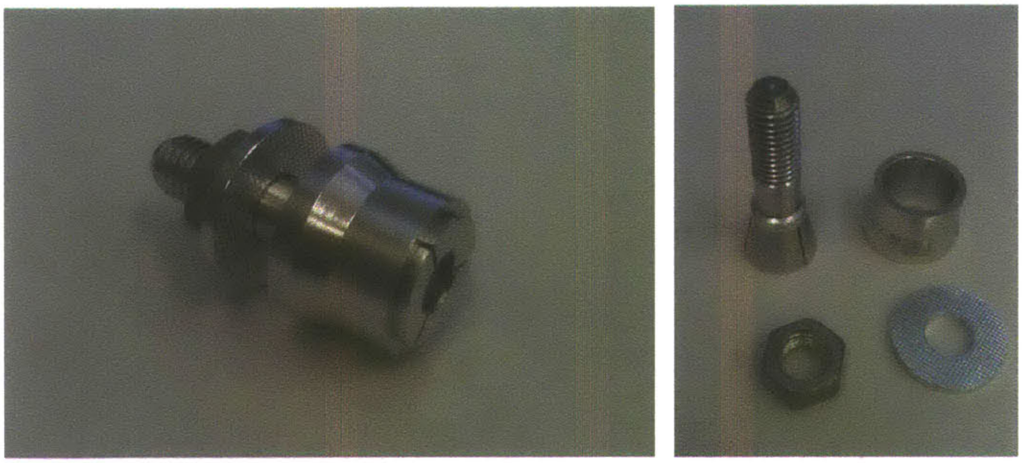
(a) (b)

Figure 4-10: Collet-type proller adaptor: a) assembled; b) components.

increase friction. The collet housing and washer/nut combination clamp over a 1/4" mounting tab inside the rotor hub, with the threaded rod running along the rotor axis. The nut is accessed through the nose of the rotor from upstream. A locking-tab washer and/or Loctite may be used to secure the nut permanently.

This method of shaft attachment is nearly identical to that used in the COTS propulsor, in which the collet and rotor are purchased as a single unit. There have been some concerns that a separately purchased collet may not be satisfactory to NASA for use with the custom propulsor because only friction secures the shaft to the collet either axially or circumferentially, and friction between the roughened washer surfaces and the rotor secures the rotor to the collet in the circumferential direction. As a result the secondary design in Fig. 4-11 has been considered. In this design, the motor shaft is threaded and has a tapered surface which interfaces with the rotor mounting tab. The primary advantage of this design is that the rotor cannot detach from the shaft without the nut coming off; in the previous attachment scheme the collet could slide axially off the motor shaft. A secondary benefit is that the method sketched in Fig. 4-11 should be self-centering, whereas with the propeller adaptor the collet shaft runs through an axial hole in the rotor hub which has some clearance which affects the centering of the rotor. Imperfect centering could lead to a rotational

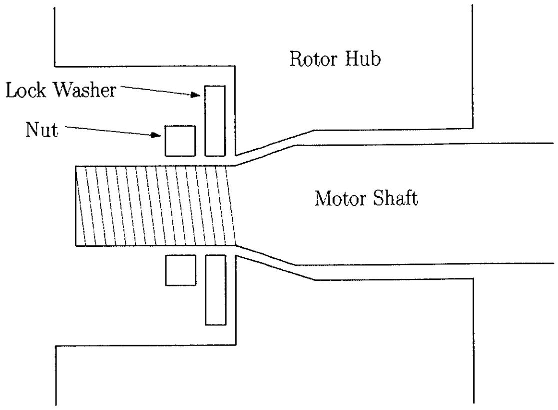

Figure 4-11: Alternative design for rotor attachment to the motor shaft.

imbalance giving rise to vibration.

The method of Fig. 4-11 requires modification of the motor shaft, which adds some complexity relative to simply purchasing a commercial propeller adaptor. It is possible that testing may alleviate some of the concerns from NASA and render the former design acceptable; if not, the method of Fig. 4-11 is suggested.

4.1.5 Nacelle Leading Edge and Static Pressure Taps

The final part required for the custom 1:11 scale propulsor is the 3D printed nacelle leading edge shown in Fig. 4-12. The internal surface contains channels parallel to the rotor axis through which the lines from the static pressure taps can be run. There are three sets of four taps each, located upstream of the rotor, between blade rows and downstream of the stator in an 'X' configuration as viewed from upstream. The taps are permanently installed in the stator, and the lines run downstream from the taps to a circumferential channel at the trailing edge of the nacelle front. They are routed around the stator and out through the hole drilled into the pylon leading edge. This configuration means that none of the taps or their pressure lines are installed in the nacelle leading edge, which can be slid axially onto the stator over the taps. This is a significant simplification over the COTS propulsor, in which taps are installed in both the FDM and metal pieces and assembly is difficult. An additional benefit is that this extends the metal stator shroud over the rotor, providing more protection

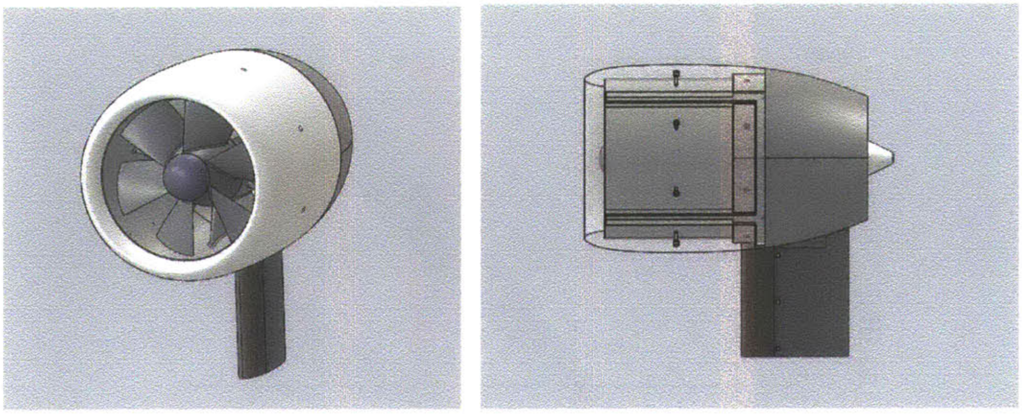
(a) (b)

Figure 4-12: Nacelle leading edge: a) installed on propulsor; b) transparent to show internal geometry.

in a blade-out instance than FDM alone. The nacelle leading edge is secured to the stator using countersunk bolts, whose heads are then clayed (or taped) over.

4.2 Structural Analysis

The majority of the detailed structural analysis required for use in the LaRC wind tunnel has yet to be carried out. Initial investigations have been conducted, however, into resonant vibration issues.

Resonant forcing in turbomachinery can be visualized using a Campbell diagram, such as in Fig. 4-13. This diagram was produced using the software in the book by Friswell et. al. [25], with appropriate values substituted for the custom 1:11 scale propulsor rotor and motor shaft. Forward and backward shaft whirl modes are plotted, along with blade resonant frequencies. The blade modes are obtained by finite element analysis (FEA) performed at Aurora Flight Sciences, while the shaft modes arise from a linear beam model in Friswell's code. Also plotted are the 1st, 2nd, 3rd, 6th and 11th engine orders. Each engine order tracks the resonant forcing due to rotation at a particular rotor speed. Forcing will be present at 6 and 11 times the rotational frequency due to the 6 rotor and 11 stator blades. Vibration may

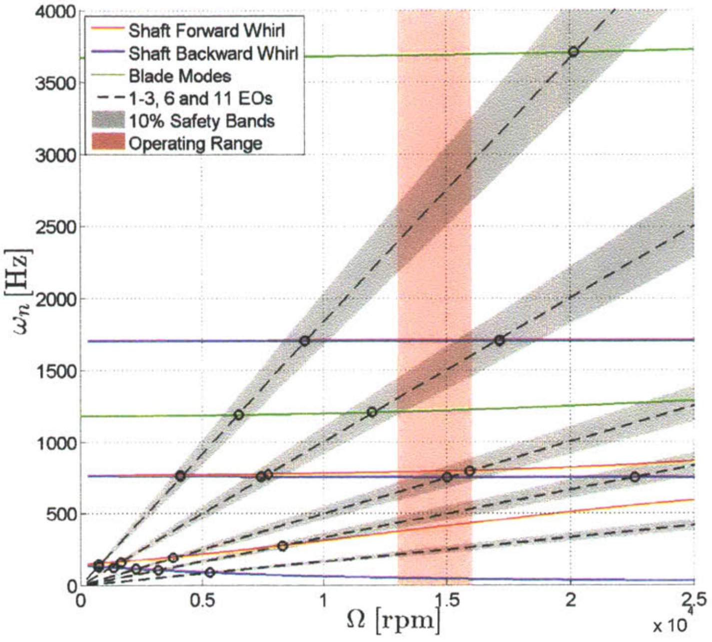

Figure 4-13: Custom 1:11 scale rotor Campbell diagram. Crossings between shaft or blade resonant frequencies and the engine order lines marked in black indicate speeds where resonant vibration may occur.

be induced by the stator due to rotor blades passing through the upstream pressure non-uniformity created by each stator blade. Investigation is ongoing into which of the low engine orders must be considered, but the first three are plotted here.

At crossings between engine orders and structural modes, there is a danger of resonance which can cause structural failure of the motor shaft or rotor blades. It is therefore desirable to operate the motor at speeds which are separated from crossings by some margin; NASA requires 10% for use in the LaRC tunnel. It can be seen that there are a large number of crossings present on Fig. 4-13. If a crossing is approached, it must be accelerated through rapidly before vibrations can grow. The desired test speed range at LaRC is plotted on Fig. 4-13 in red. There are at least two crossings of concern, involving the third engine order and second shaft mode.

There is a large uncertainty in the results in Fig. 4-13 because of uncertainty in the prediction of the shaft modal frequencies. The motor shaft is mounted on two ball bearings at the front and rear of the motor cylinder. Its resonant frequencies are dependent on the radial stiffness of these bearings, which affects the location of crossings with the various engine orders. Reference [26] provides a method for computing this radial bearing stiffness as

$$K_r = \frac{(FD_bZ^2)^{1/3}}{1.275 \times 10^{-7}}\,. \tag{4.1}$$

D_b and Z are the diameter and number of the ball bearings, respectively, and the constant in the denominator is empirical. Eq. 4.1 is non-linear and dependent on the bearing radial load, F, which is a function of rotor speed and imbalance. The imbalance in the rotor is unknown a priori, as are the effects of internal clearances in the ball bearings [26]. The result is that K_r is not known well enough to give confidence in the results of Fig. 4-13, which was produced using Eq. 4.1 and the bearing loads at zero rotational speed which can be computed from a static force balance. This neglects the dependency of K_r on Ω, which will serve to increase bearing stiffness during rotation.

It is unclear how radial bearing stiffness during rotation might be measured and an alternative strategy is to measure crossings on the Campbell diagram directly. If a representative rotor is manufactured from an aluminum disk with the same mass properties as the custom rotor and affixed to the motor shaft in the same location, the resonant frequencies of the shaft should approach those which will be seen during wind tunnel testing. An accelerometer mounted to the rotor case while the motor is run to its full test speed can detect crossings on the Campbell diagram as spikes in a fast-Fourier transform (FFT) plot of its data. The advantage of using a representative rotor is that the real machined part is not risked; only the motor, which is of much lower cost, would be damaged during a failure due to vibration. The drawbacks of this method are that the imbalance of the rotor may not be matched by the representative disk, and that blade modes cannot be captured. Fig. 4-13 shows, however, that blade modes should be of less concern than shaft modes, and various degrees of imbalance could be explored using different representative rotors.

The proposed test is suggested in advance of operation of the custom propulsor with an installed rotor. Safety precautions should include use of a protective outer casing to contain parts in the event of a shaft failure, and attempts to detect static shaft modes using a ping test before beginning motor rotation. This may allow insight into expected crossing areas, as does Fig. 4-13.

Additional steps taken to alleviate vibration concerns include tailoring of the shaft stiffness and rotor mass and axial location. The lower the rotor mass and the closer the center of gravity to the upstream motor bearing, the higher the natural frequencies of the shaft modes. Increasing modal frequencies delays crossings on the Campbell diagram, and effort has been made to minimize rotor mass and overhang. Further steps may be taken in this direction pending the results of the test described above. Stiffening of the shaft by increasing its diameter or the use of high carbon steel is also beneficial. The diameter may be maximized by magnetizing the shaft itself and eliminating the need for additional permanent magnets as are normally required in a brushless DC motor. This is discussed further in Chapter 5.

4.3 Conclusions

A preliminary structural layout of the 1:11 scale custom propulsor has been completed. Some details remain to be defined or iterated, including the sizing of fasteners and fillets and iteration of the turbomachinery blading. The design is based on the existing 1:11 scale COTS propulsor, but offers improvements in assembly and access to the motor, plug and pressure taps. Detailed structural analysis is still to be completed, and is required for use in the LaRC wind tunnel. Some initial work on shaft vibration issues has been carried out, and a test has been proposed to map crossings on the Campbell diagram.

Chapter 5

Electric Motor Calibration and Testing

As previously stated, a goal of the N+3 wind tunnel tests is assessment of the propulsive benefit of boundary layer ingestion. One expected effect of BLI will be a change in isentropic fan efficiency as a result of operation with inlet distortion. In our assessment of BLI benefits, it is of central importance to determine the $\Delta\eta_f$ between the podded and integrated configurations. We define $\eta_f \equiv {}^{P_{flow}}/_{P_{shaft}}$, where P_{flow} is determined as [5]

$$P_{flow} = \oiint - \left[(p - p_\infty) + \frac{1}{2}\rho\left(V^2 - V_\infty^2\right)\right] \vec{V} \cdot \hat{n} dA\,. \tag{5.1}$$

In addition to P_{flow}, the electrical power input into the propulsor motors will be measured during testing. The motor efficiency $\eta_m \equiv {}^{P_{shaft}}/_{P_{electric}}$ varies with motor speed, torque and temperature as well as potentially with manufacturing differences between motors and controllers of the same model. It is necessary to know η_m to extract η_f because $P_{flow} = \eta_f\, \eta_m\, P_{electric}$. Motor efficiency is computed from

$$\eta_m = \frac{Q_m \Omega}{iv}\,. \tag{5.2}$$

The current i and voltage v are measured at the motor controller terminals and Ω

is determined by monitoring the oscillating counter-electromotive force (back EMF). The torque, Q_m, is unknown. The initial plan was to measure Q_m directly by mounting the motor flexibly in bearings which did not resist circumferential rotation. A small load cell embedded in the propulsor centerbody made contact with the motor at a single point offset from the axis of rotation by a known moment arm, preventing rotation. The known moment arm and measured force would provide motor torque. Unfortunately, it was found that heat generated by the motor caused the load cell reading to drift and the torque meter response could not be relied on.

Brushless DC electric motors, in general, however, are repeatable devices which can be expected to operate at the same η_m given the same Ω, Q_m and coil temperature [27]. It is therefore possible to perform motor calibrations, at the operating points of interest, separate from the NASA wind tunnel tests. These are described below along with a review of the basics of DC electric motor function.

5.1 DC Electric Motor Fundamentals

5.1.1 Conventional DC Motors

All DC electric motors function by creating two magnetic fields with misalignment between them. Rotation is then induced in such a way as to bring the two fields into alignment. In a conventional permanent magnet 'brushed' DC motor, sketched in Fig. 5-1(a), the motor contains a set of permanent magnets, known as stators, which establish a constant magnetic field. The rotor consists of a set of coils wrapped around a ferromagnetic core which becomes an electromagnet when current is induced in the coils [28]. The current enters the coils via small conductive brushes which typically extend radially inward to contact a commutator mounted on the shaft. The commutator consists of a set of conductive surfaces, each of which is electrically connected to some of the coils but not to the other commutator surfaces. The number of coils (and hence the number of surfaces composing the commutator) is referred to as the number of poles and varies with motor design.

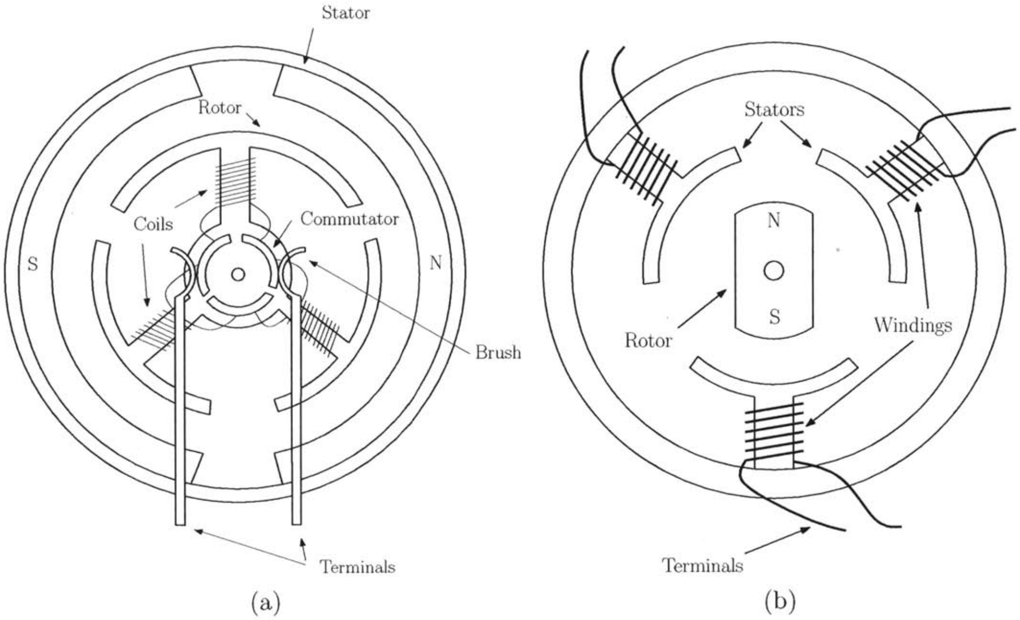

Figure 5-1: DC electric motor geometry: a) conventional; b) brushless.

The motor internal geometry is such that when the brushes complete a circuit with the commutator, current is induced in the windings so the generated rotor electromagnetic field is out of phase with the stator field and a rotational force is produced to bring the fields into alignment. As alignment is approached, however, the brushes break contact with a particular commutator surface and contact the next, altering the generated rotor field, which permanently lags the stator field to maintain rotation. To increase rotational speed, a higher DC voltage is applied to the motor terminals and hence the windings. Disadvantages of internally-commutated designs include the tendency of the brushes to break, spark and fail, and to produce internal friction losses which lower motor efficiency. The brushless DC motors described in Section 5.1.2 avoid these failings.

5.1.2 Brushless DC Motors

A brushless DC (BLDC) electric motor is shown in Fig. 5-1(b). In a BLDC motor it is the rotor which contains the permanent magnets, which are typically bonded to a metal shaft. The stator consists of sets of electrically independent wire coils distributed around the inside of the motor which induce electromagnetic fields of varying alignment when current is applied to them individually. These coils connect to separate motor terminals and to an external electronic speed controller (ESC) which serves as both a voltage reducer via pulse-width modulation (PWM) and an external commutator [29]. The ESC monitors the back EMF along each of the lines connecting it to the motor and activates the independent coils so that the induced magnetic field is permanently out of alignment with the rotor field. The rotor thus chases the moving stator field to maintain rotation. Increased rotational speed is achieved by applying a higher voltage to the motor terminals, typically by increasing the duty-cycle supplied by the ESC.

For the ESC to switch the correct coils on and off at the proper time, it must know the alignment of the rotor magnetic field, and hence the angular position of the rotor. In the ESCs currently used, this is achieved by leaving gaps in the PWM signal during which voltage is not applied to the motor and rotation is maintained by inertia. During these gaps in the signal, the motor functions as a generator in which a permanent magnet spins inside a set of conductive coils [28]. This induces current in the windings, with the observed voltage during this period directly proportional to the angular speed at which the motor is turning. The induced voltage, which is the back-EMF generated by the changing magnetic field, is used by the ESC to monitor rotor angular position and govern commutation of the coils.

In our configuration, a constant voltage source is connected to the ESC, which is then connected to the motor terminals. The action of the ESC results in an alternating current in each of the motor wires, which is out-of-phase with the current in the other wires. The phase difference generates the rotating stator magnetic field; the voltage at the motor terminals resembles a sine wave broken up by the PWM signal and position-monitoring lags.

Because of timing differences in the back-EMF generation or monitoring, there can be a variation in the performance of individual motor/ESC combinations of the same model [23]. Brushless DC motors have no physical connection between rotor and stator and tend to outlast and outperform brushed motors. The most common source of failure in these motors occurs when the core temperature becomes high enough that the glue attaching the permanent magnets of the rotor to the shaft fails [30]; this is what typically occurs when a motor 'burns-out.' The risk of burnout can be alleviated by monitoring motor temperature, by the use of high-temperature glue or by permanently magnetizing the shaft and eliminating the need for externally attached magnets. For the electric motors used in the COTS propulsor, neither of these last two steps have been taken and it is important to monitor the temperature inside the motor core to prevent burnout. The temperature also affects motor performance through changes in the resistance of the stator coils [31].

It is difficult to measure internal motor temperature directly. A thermocouple cannot be attached to the stator coils without affecting their electrical properties, nor can one be attached to the rotor. An alternative is to measure motor skin temperature from thermocouples attached to the exterior of the motor. The temperature above ambient will be proportional to the temperature rise of the stator coils and the rotor. If the exterior of the motor is uncooled, or insulated, the skin, coil and rotor temperatures may become close, but in the envisioned operation there is heat removal to prevent overheating. Cooling, whether it relies on air or water, removes heat from the motor skin and affects the relationship between the temperature measured here and the relevant core temperatures. Estimation of thermal effects on motor performance has been a challenge in motor calibration, as discussed in Sec. 5.4.

5.2 Dynamometer Testing

A small dynamometer has been designed and constructed to measure torque during motor operation. A schematic of the dynamometer is given in Fig. 5-2. The motor is mounted on bearings so that rotation is prevented only by a force on a known moment arm acting through a load cell. The moment arm is sufficiently long that the load cell does not experience thermal effects from motor waste heat. The motors can be calibrated on this stand to determine their efficiency at the relevant operating points.

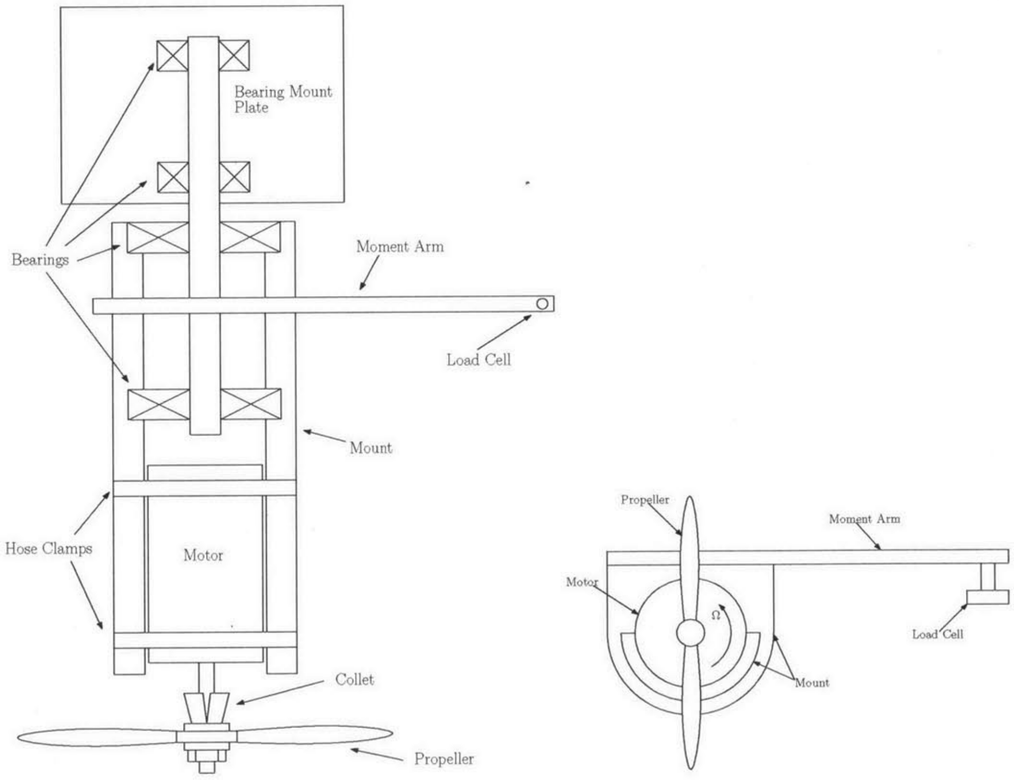

(a) (b)

Figure 5-2: Dynamometer used to measure COTS motor rotating torque.

In the remainder of this chapter the results from tests performed with this apparatus on the Lehner 3040-27 motors used in the COTS nacelle will be described. Predicted COTs propulsor operating points for the LaRC wind tunnel, in a graph of torque versus rotor speed, are shown on Fig. 5-3 in black. There are 18 points, corresponding to a matrix of three nozzle areas and three power settings for each configuration. Commercially available RC aircraft propellers were used to provide torque loads that bracketed the operating points. The measured torque-speed curves of the propellers are denoted on Fig. 5-3 by colored points. Combined motor/ESC efficiencies were measured along the propeller torque-speed curves and at various temperatures. A matrix of motor/ESC combinations has been calibrated for the COTS nacelle to determine differences between the combinations.

The calibration matrix for the motors is presented in Table 5.1. It has been chosen to allow up to two motor or ESC failures during LaRC testing while leaving a calibrated set for each propulsor.[1] Calibration results from the combinations indicated in Table 5.1 are given in Figs. 5-4 through 5-7 and Table 5.2. The contour plots are obtained by averaging approximately 10 seconds of data at each motor speed with each propeller. The data was taken after transients between the steps were completed (during acceleration, the motor performs at a reduced efficiency which is not of interest).

It was discovered during the last stages of writing that calibrations were inadvertently performed with the motor spinning in the opposite direction of that intended for the LaRC tests. Comparison to data taken by Titchener (Table 5.3) [32] using the opposite direction of spin has therefore been made to evaluate the difference. The propellers in the tests of Table 5.2 were rotated trailing edge first, to reduce the thrust load on the measurement apparatus and provide higher torques to match the expected LaRC operating points. In Titchener's results the propellers were rotated leading edge first, meaning the measurements were taken along slightly different torque-speed curves. The maximum difference is 2.2%. It is emphasized, however,

---

[1] Additional motor calibrations beyond those presented here have also been performed using this same test apparatus by Titchener [32].

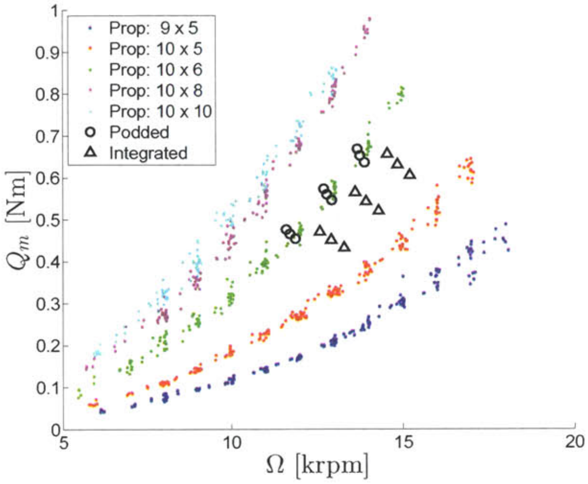

Figure 5-3: Target COTS LaRC operating points and torque vs. speed curves for various propellers measured by dynamometer.

ESC	Motors			
No.	6	7	11	12
1	X			
3		X		
4	X	X	X	X
5			X	

Table 5.1: Motor/ESC calibration matrix. Numbering corresponds to internal N+3 project labeling.

that the repeatability of the calibration needs further investigation as discussed in Sec. 5.4.

Table 5.2 shows that the combined motor/ESC efficiencies at the expected operating points are in the range of 74-83%. On average the motors operate 2.0% more efficiently at operating points corresponding to the integrated configuration rather than the podded.

Efficiency differences between motors and ESCs are small, with the largest standard deviation between separate calibrations at any of the operating points equal to 1.2%. Some of the differences in Table 5.2 may be due to variation in motor temperature, which is measured via a skin-mounted thermocouple. The motors are insulated

		Motor-ESC Combination								
krpm	Q_m	6-1	6-4	7-3	7-4	11-4	11-5	12-4	$\bar{\eta}_m$	σ
11.6	0.48	0.749	0.754	0.756	0.752	0.756	0.752	0.753	0.753	2.1e-3
11.7	0.47	0.750	0.756	0.757	0.744	0.754	0.748	0.750	0.751	3.9e-3
11.9	0.45	0.739	0.743	0.760	0.742	0.750	0.741	0.755	0.747	7.0e-3
12.7	0.57	0.759	0.759	0.774	0.787	0.781	0.766	0.777	0.772	9.5e-3
12.8	0.56	0.757	0.758	0.774	0.783	0.784	0.767	0.777	0.772	9.6e-3
12.9	0.55	0.754	0.750	0.780	0.775	0.781	0.761	0.773	0.768	1.1e-2
13.7	0.67	0.793	0.790	0.809	0.802	0.789	0.799	0.800	0.798	6.1e-3
13.8	0.65	0.795	0.791	0.810	0.800	0.788	0.798	0.800	0.797	6.2e-3
13.9	0.64	0.795	0.793	0.811	0.796	0.788	0.797	0.801	0.797	6.2e-3
12.6	0.47	0.752	0.757	0.770	0.774	0.770	0.755	0.770	0.764	7.8e-3
12.9	0.45	0.744	0.742	0.777	0.759	0.773	0.754	0.770	0.760	1.2e-2
13.3	0.43	0.778	0.774	0.790	0.771	0.768	0.773	0.776	0.776	6.2e-3
13.6	0.57	0.789	0.784	0.806	0.791	0.781	0.789	0.792	0.790	6.9e-3
13.9	0.54	0.788	0.786	0.810	0.785	0.787	0.788	0.796	0.791	7.6e-3
14.3	0.52	0.790	0.814	0.811	0.808	0.792	0.794	0.815	0.803	9.4e-3
14.5	0.66	0.806	0.813	0.815	0.819	0.797	0.810	0.818	0.811	6.7e-3
14.9	0.63	0.809	0.820	0.819	0.825	0.800	0.813	0.823	0.815	7.8e-3
15.2	0.61	0.816	0.823	0.814	0.821	0.811	0.838	0.838	0.823	9.5e-3
$\bar{\eta}_{m,pod}$		0.766	0.766	0.781	0.776	0.775	0.770	0.776	0.773	5.0e-3
$\bar{\eta}_{m,BLI}$		0.786	0.790	0.801	0.795	0.787	0.790	0.800	0.793	5.3e-3

Table 5.2: Measured η_m for seven motor/ESC combinations. $\bar{\eta}_m$ is the average efficiency and σ is the standard deviation of the measured efficiency at each operating point across combinations. Rows 1-9 correspond to the podded aircraft configuration and 10-18 to the integrated configuration.

kRPM	Q_m	$\eta_{m,\text{rev}}$	$\eta_{m,\text{for}}$	$\Delta\eta_m$
11.60	0.48	0.752	0.769	2.18%
11.71	0.47	0.752	0.762	1.26%
11.86	0.45	0.741	0.752	1.50%
12.69	0.57	0.762	0.766	0.53%
12.78	0.56	0.760	0.763	0.39%
12.92	0.55	0.757	0.760	0.41%
13.67	0.67	0.796	0.793	0.45%
13.75	0.65	0.798	0.789	1.18%
13.88	0.64	0.798	0.787	1.38%
12.58	0.47	0.754	0.761	0.93%
12.91	0.45	0.747	0.754	0.95%
13.29	0.43	0.780	0.771	1.26%
13.61	0.56	0.792	0.779	1.62%
13.92	0.54	0.791	0.779	1.55%
14.29	0.52	0.793	0.806	1.58%
14.54	0.66	0.809	0.803	0.73%
14.85	0.63	0.812	0.805	0.79%
15.21	0.60	0.819	0.803	1.99%
			Avg.	1.15%
			Max	2.18%

Table 5.3: Comparison of data taken using forward and reverse rotation directions with motor #6 and ESC #1. Forward rotation data from Titchener.

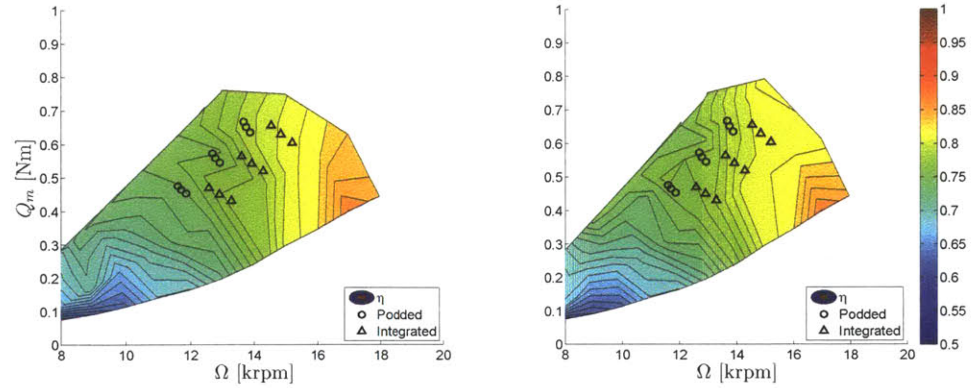

(a) (b)

Figure 5-4: Motor #6 efficiency contours: a) ESC #1; b) ESC #4.

during calibration so as to equalize the skin and core temperatures; this is possible without overheating due to the limited duration of these tests (approximately 10 minutes per propeller).

Representative plots of skin temperature and ESC duty-cycle are shown in Fig. 5-8. Motor performance is known to vary with core temperature [31], and ESC efficiency is known to depend on duty-cycle [14]. The temperatures obtained during testing at LaRC inside the nacelle may not match the calibration range of the dynamometer tests, and a method for extrapolating the torque prediction beyond the current data is described in Section 5.3.

5.3 Motor Analysis

A possible method for extrapolation of torque information is based on the second-order DC electric motor analysis developed by Drela [31] for brushed DC motors. The torque is represented as a function of the current i and rotational speed Ω as

$$Q_m(i,\Omega) = {}^{(i-i_0)}/_{K_Q}\,, \qquad (5.3)$$

$$i_0(\Omega) = i_{0_0} + i_{0_1}\Omega + i_{0_2}\Omega^2\,. \qquad (5.4)$$

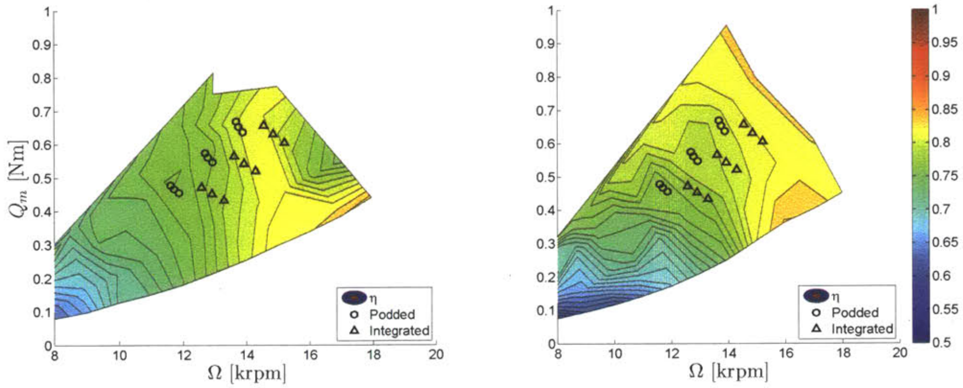

(a)

(b)

Figure 5-5: Motor #7 efficiency contours: a) ESC #3; b) ESC #4.

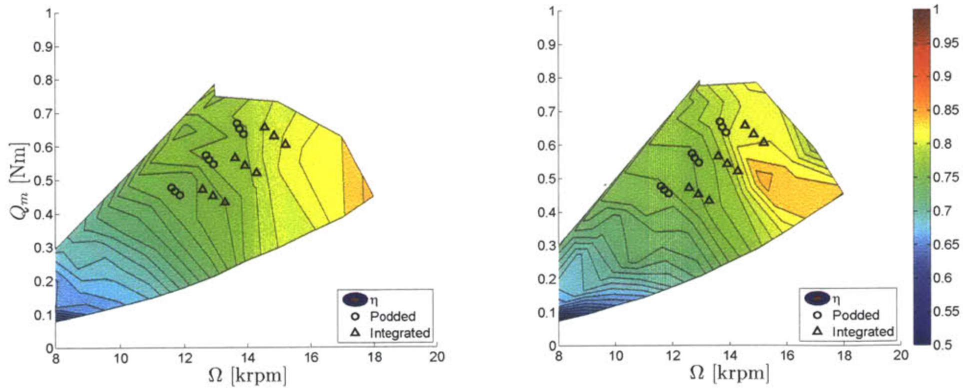

(a)

(b)

Figure 5-6: Motor #11 efficiency contours: a) ESC #4; b) ESC #5.

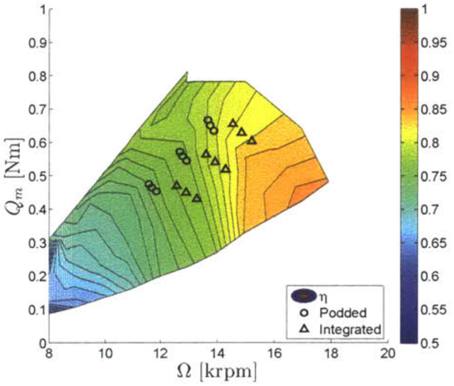

(a)

Figure 5-7: Motor #12 efficiency contours: ESC #4.

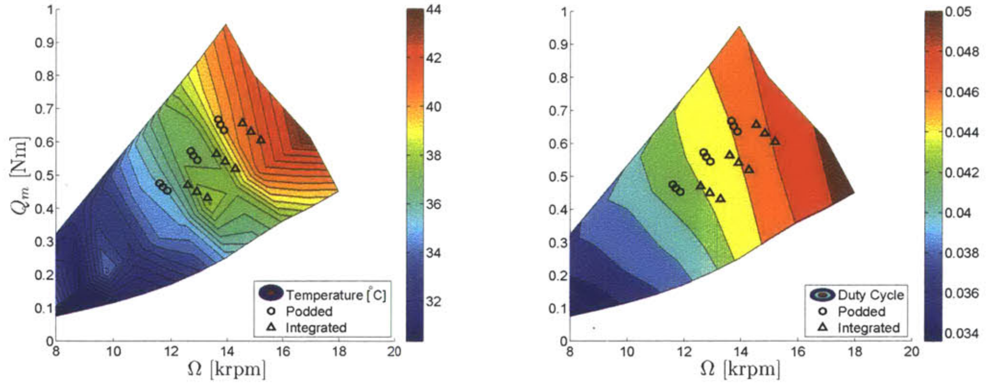

(a) (b)

Figure 5-8: Motor #7 ESC #4: a) motor skin temperature; b) ESC duty-cycle.

The parameter K_Q is a motor torque constant in units of Amp/Nm and i_0 is the zero-torque current. The constant i_{0_0} captures the effect of sliding friction in the rotor bearings and brushes, and i_{0_1} and i_{0_2} capture laminar and turbulent air resistance to the rotor, respectively. Current and Ω are measured directly and it is the constant coefficients that are not known. The model must also be modified to account for the action of the ESC. To do this it is suggested by Moffitt [14] that ESC efficiency can be represented as a linear function of the PWM duty-cycle:

$$\eta_{ESC} = 1 - k_{loss} \left(D_{\mathrm{c,\ max}} - D_c\right) . \tag{5.5}$$

Here k_{loss} determines how rapidly the efficiency decays with decreasing duty-cycle and Moffitt suggests 0.078 as a typical value [14].

The effect of temperature must also be accounted for. A suggested behavior is

$$\eta_{temp} = 1 - t_1 \left(T_{skin} - T_{ref}\right) . \tag{5.6}$$

A linear description of temperature effects is suggested by Drela [31] and borne out by tests of the same motor/ESC combination at a range of temperatures. Eq. 5.6 may be extended to higher order functions of $(T_{skin} - T_{ref})$, but for the data examined this does not yield increased accuracy.

Eqs. 5.3 through 5.6 provide a means for shaft torque (and hence combined motor/ESC efficiency) to be estimated from measurements of i, Ω, D_c and T_{skin} using the eight calibration constants K_Q, i_{0_0}, i_{0_1}, i_{0_2}, k_{loss}, $D_{\mathrm{c,\ max}}$, t_1 and T_{ref}. Simultaneous optimization of the eight constants for each motor/ESC combination was used to match the model to the approximately 55 data points collected during each calibration. Estimates suggested by Drela [31] and Moffitt [14] were used to inform the optimizer start point and set bounds, although as with all gradient-based optimizations the use of multiple start points is necessary to assist convergence to an acceptable optimum. The MATLAB gradient-based optimization function `fmincon` [22] was used to minimize the difference between the measured and predicted torques at the

Cal.	Motor-ESC Combination						
Const.	6-1	6-4	7-3	7-4	11-4	11-5	12-4
K_Q	30.33	29.90	29.69	29.18	30.81	28.85	30.35
i_{0_0}	0.103	0.187	0.100	0.100	0.100	0.102	0.143
i_{0_0}	-6.62e-3	-6.05e-3	-6.63e-3	-6.09e-3	-6.93e-3	-5.58e-3	-6.39e-3
i_{0_0}	5.00e-6	4.45e-6	4.96e-6	5.00e-6	5.00e-6	4.49e-6	4.76e-6
k_{loss}	0.092	0.092	0.078	0.075	0.077	0.099	0.070
$D_{c\ \max}$	0.090	0.089	0.090	0.090	0.091	0.090	0.090
t_1	0.002	0.003	0.003	0.003	0.003	0.003	0.003
T_{ref}	10.05	10.01	10.00	13.15	10.00	10.00	10.28
Avg. $\Delta\eta_m$	0.55%	0.58%	0.54%	0.73%	0.73%	0.50%	0.36%
Max $\Delta\eta_m$	1.57%	2.34%	2.10%	2.07%	2.02%	1.78%	1.15%

Table 5.4: Motor/ESC calibration factors. $\Delta\eta_m \equiv \eta_{m,\text{meas}} - \eta_{m,\text{pred}}$ at the 18 expected LaRC COTS operating points.

expected operating points according to

$$\min \Delta Q_{\text{avg}} = \text{mean}\left(\text{Q}_{\text{m, measured}} - \text{Q}_{\text{m, predicted}}\right) . \tag{5.7}$$

The resulting calibration factors are given in Table 5.4. The agreement is good, with $\Delta\eta_m = 2.34\%$ the largest discrepancy between a predicted and measured efficiency value. A sample plot of predicted η_m is included for the motor #7 - ESC #4 combination in Fig. 5-9 for comparison with the data in Fig. 5-5(b).

5.4 Uncertainty and Repeatability

Repeatability has yet to be examined as fully as needed and it is planned that ongoing work by Titchener will address this issue. To date, repeatability has been examined only by comparing the results of two calibrations performed on separate days as shown in Table 5.5. The largest disagreement found is approximately 1.94%, but more repeat runs are required.

There are several possible origins for this uncertainty, arising from the experimental set-up and measurement equipment. The repeatability rating of the load cell is ±0.1% of its full rated load [33], which translates to approximately ±0.8% in mea-

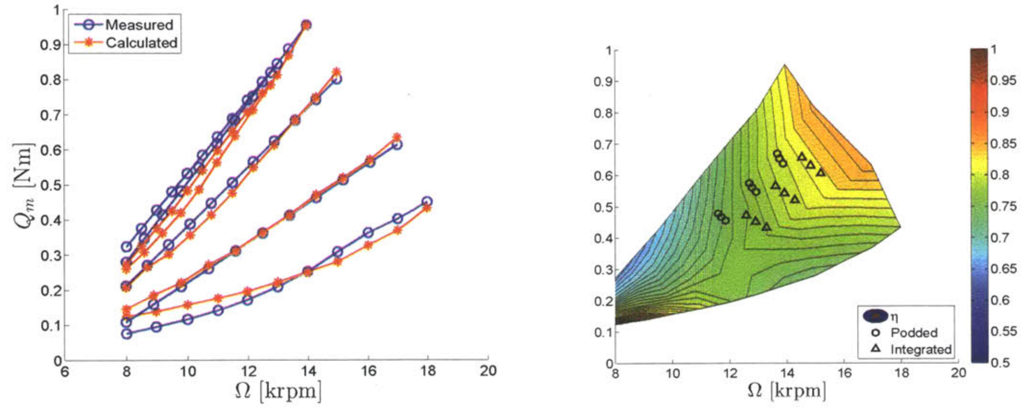

(a) (b)

Figure 5-9: Motor #7 ESC #4: a) calculated and measured torque values; b) contours of efficiency given by the motor analysis.

sured efficiency at the load levels experienced in these tests, and it is recommended a more accurate load cell be obtained for use in future calibrations.

5.4.1 Measurement Unsteadiness

Uncertainty in the measurements arises from fluctuations in measured motor speed. Five minutes of data are shown in Fig. 5-10(a) after a settling time of ten minutes. The standard deviations are 0.015 V and 50.3 rpm. This level of fluctuation is seen throughout the calibrations regardless of the time allowed for the motor to settle. This may be the result of either an inaccurate reading of the motor speed, the action of the proportional-integral-derivative (PID) controller used to set the speed, or a fundamental inability of the motor and ESC combination used here to hold a more constant rotational speed. It has been suggested by Moffitt that higher quality controllers manufactured by JETI may be be able to hold a tighter speed tolerance than those currently used [27].

There are fluctuations in the raw load cell reading, which do not follow the fluctuations in speed. The differences are likely a result of the data acquisition method. The algorithm averages load cell data internally over two second intervals, and samples

kRPM	Q_m	$\eta_{m,a}$	$\eta_{m,b}$	$\Delta\eta_m$
11.60	0.48	0.756	0.765	1.18%
11.71	0.47	0.757	0.767	1.30%
11.86	0.45	0.760	0.775	1.94%
12.69	0.57	0.774	0.780	0.77%
12.78	0.56	0.774	0.782	1.02%
12.92	0.55	0.779	0.785	0.76%
13.67	0.67	0.809	0.821	1.46%
13.75	0.65	0.810	0.820	1.22%
13.88	0.64	0.811	0.819	0.98%
12.58	0.47	0.770	0.784	1.79%
12.91	0.45	0.777	0.789	1.52%
13.29	0.43	0.790	0.796	0.75%
13.61	0.56	0.806	0.811	0.62%
13.92	0.54	0.810	0.808	0.25%
14.29	0.52	0.811	0.807	0.50%
14.54	0.66	0.815	0.823	0.97%
14.85	0.63	0.819	0.821	0.24%
15.21	0.60	0.814	0.821	0.85%
			Avg.	1.01%
			Max	1.94%

Table 5.5: Comparison of calibration runs using motor #7 and ESC #3 on different days.

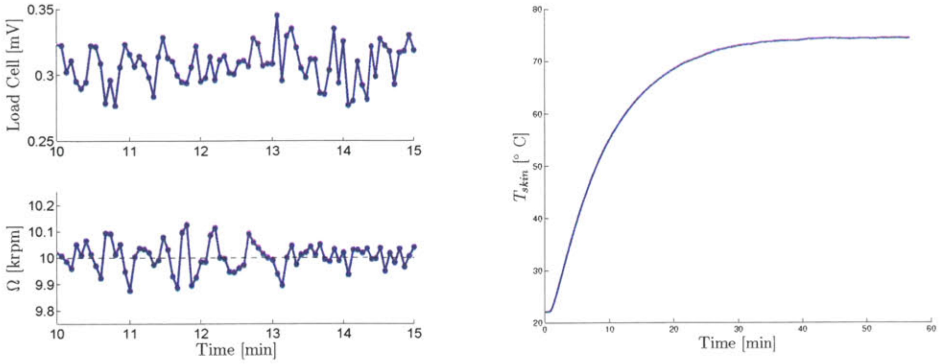

(a) (b)

Figure 5-10: Motor test to thermal equilibrium: a) fluctuation in load cell (above) and motor speed (below) readings; b) approach to thermal equilibrium.

the speed over 0.2 second intervals every two seconds. For future tests it is recommended that the data acquisition software be modified to store measurements at a higher frequency and to sample speed and load cell readings simultaneously. Some of the unsteadiness in the load cell data may also be due to the effect of airflow from the propeller on the dynamometer moment arm. The effect of these variations in speed and load reading are presently handled by time averaging.

5.4.2 Thermal Effects

Additional uncertainty arises from the effects of temperature on the motor performance. Fig. 5-10(b) shows that the motor takes nearly 40 minutes to reach thermal equilibrium at a given operating point. This makes it impractical to obtain the number of data points required for motor calibration at thermal equilibrium. Further it is likely that during data acquisition in the LaRC wind tunnel the motor may not reach thermal equilibrium at many operating points. As a result, data was acquired after allowing only the speed to settle (to within the limits indicated on Fig. 5-10(a)). Fig. 5-8(a) shows that this results in calibration runs in which the motor temperature varies. In fact the temperature is rising slightly over the duration of the data acquisition at each (Ω, Q_m) point, which means the performance is changing. Again this is presently handled by time averaging.

More significantly, it has been difficult within the time constraints to heat the motor from room temperature to the levels at which it is expected to operate during the LaRC tests (approximately 60°C), and the calibrations presented here have been performed at temperatures ranging from 25-45°C. The validity of extrapolation using Eqs. 5.3 through 5.6 has been checked by calibrating a single motor/ESC combination at a low temperature, and using the analytical model to estimate the behavior at higher temperature. Comparison of the extrapolation with data taken at the highest temperature which it has thus far been possible to achieve during a full calibration is shown in Table 5.6 and Fig. 5-11. Data was extrapolated from a mean temperature of 32.5°C to 46.6°C, and the largest disagreement between the data and the prediction at any of the operating points was $\Delta\eta_m = 3.5\%$. Fig. 5-11 shows that the agreement is best near the LaRC operating points because the model is optimized for agreement in this range according to Eq. 5.7. Additional comparisons between extrapolated and measured data would be beneficial, although ideally all the calibrations would be carried out at high temperature. The use of an external heating element such as a heat gun or space heater could aid temperature control.

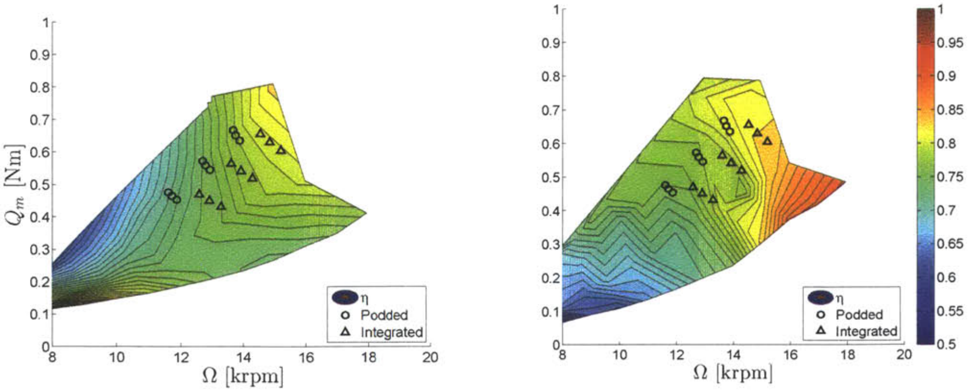

(a)

(b)

Figure 5-11: Temperature extrapolation with motor #7 and ESC #3: a) calculated efficiency at 46.6°C based on calibration at 32.5°C mean temperature; b) measured efficiency at 46.6° mean temperature.

kRPM	Q_m	$\eta_{m,\text{ meas}}$	$\eta_{m,\text{ calc}}$	$\Delta\eta_m$
11.60	0.48	0.742	0.721	2.76%
11.71	0.47	0.738	0.728	1.32%
11.86	0.45	0.732	0.738	0.79%
12.69	0.57	0.762	0.751	1.48%
12.78	0.56	0.760	0.751	1.10%
12.92	0.55	0.756	0.753	0.37%
13.67	0.67	0.797	0.783	1.76%
13.75	0.65	0.797	0.785	1.45%
13.88	0.64	0.794	0.784	1.26%
12.58	0.47	0.749	0.750	0.12%
12.91	0.45	0.743	0.752	1.20%
13.29	0.43	0.753	0.763	1.29%
13.61	0.56	0.786	0.774	1.54%
13.92	0.54	0.779	0.774	0.61%
14.29	0.52	0.771	0.781	1.37%
14.54	0.66	0.787	0.811	3.10%
14.85	0.63	0.788	0.815	3.46%
15.21	0.60	0.803	0.817	1.76%
			Avg.	1.49%
			Max	3.46%

Table 5.6: Temperature extrapolation with motor #7 and ESC #3: comparison of calculated vs. measured efficiency at 46.6°C mean temperature. Calculation based on calibration at 32.5°C mean temperature.

Another uncertainty exists in the application of the calibration factors to data acquired in the LaRC wind tunnel. The motor core temperature determines performance and the motors in these calibrations were therefore insulated to equalize the core temperature and the measured skin temperature. In the wind tunnel tests, the motors will be cooled to prevent overheating, introducing uncertainty in the core temperatures. The relationship between skin and core temperature is a function of the thermal environment present inside the nacelle, and cannot be replicated on the test stand. Work has been done by Siu [34] to estimate this relationship by running the motor at a particular operating point, then shutting it off and observing the measured temperature spike as the skin and core temperatures equalize in the absence of cooling. At the time of writing, however, the data has not yet been fully analyzed.

In sum, the most worrisome uncertainty appears to be the effect of temperature on efficiency which is difficult to evaluate with the current set-up. High temperatures (near 100°C) also place the motors in danger of burnout.

The current best estimate of the absolute uncertainty in efficiency is ±2.5% when the motors are operated at temperatures near where they were calibrated, derived from a comparison of the agreement found in Tables 5.2, 5.3, 5.4 and 5.5. Table 5.6 gives information on uncertainty arising from extrapolation over different temperatures.

5.5 Conclusions

A dynamometer appropriate for measuring the rotating torque of small electric motors has been designed, constructed, and used to carry out calibration of seven motor/ESC combinations. The uncertainty in measured efficiency is estimated at ±2.5%. The differences between different motor/ESC combinations were no larger than 1.5%. An analysis, developed to allow extrapolation of measured efficiencies to other operating points, gave calculated efficiencies within ±2.4% when the motor was operated below 40°C. Motor efficiency was also found to decrease with temperature; for an average temperature increase of 14.1°C the average efficiency decreased by 2.2%.

Chapter 6

Summary, Conclusions and Suggestions for Future Work

An MIT, Aurora Flight Sciences and Pratt & Whitney team, in collaboration with NASA and as part of the NASA N+3 program, is examining aircraft and propulsion concepts for future civil transports. A configuration of particular interest is fuselage boundary layer ingestion (BLI) by engines mounted above a widened fuselage. Wind tunnel experiments are planned to assess the benefits of BLI from this configuration. The experiments are to be conducted at the NASA Langley Research Center (LaRC) and at MIT, with powered 1:11 and 1:4 scale models that use electric fans to simulate the engines. Two different propulsor stages are used, a 'commercial off-the-shelf' (COTS) turbomachine and a custom propulsor fan stage. This thesis describes contributions to the analysis, design and characterization of these representative engine simulators.

6.1 Summary and Conclusions

1. Scaling arguments have been presented in support of the selection of electric motors for the 1:11 and 1:4 scale models, including the cooling requirements. It has been found, from the work in the thesis and the comparison with work by Hall [9], that the motor requirements are robust to the selection of scaling

parameters used to determine model propulsor characteristics.

2. Aerodynamic design of the 1:11 scale podded aircraft configuration propulsor nacelle and centerbody has been carried out using a gradient-based optimizer and axisymmetric interacting boundary-layer theory solver. Eight centerbody trailing edge plugs for the 1:11 scale COTS propulsor have also been designed using the optimization tool. These plugs are of a range of sizes to enable propulsor mass flow variations up to 40%, at a given rotor speed.

3. A preliminary structural design of the custom 1:11 scale podded propulsor has been carried out. The design is informed by the existing 1:11 scale COTS propulsor, but offers improvements in terms of assembly and access to plugs, pressure taps and the electric motor. Rotational speeds which may produce resonant vibration in the rotor have been identified on a Campbell diagram. An experimental method of directly measuring crossings on the Campbell diagram has been proposed to provide appropriate assessment of these resonant frequencies.

4. Efficiencies of the brushless DC electric motors and controllers used in the 1:11 scale COTS propulsor have been measured over the range of expected LaRC operating points. A dynamometer has been designed and constructed to measure motor torque, and measurements were obtained with different motor and controller combinations at the target operating points. An analytical model was developed which matches the experimental data to within 2.4%. The differences in average efficiency between motors and controllers were less than 1.5%. Motor efficiency was found to decrease with motor temperature; for an average temperature increase of 14.1°C the average efficiency decreased by 2.2%.

5. A wind tunnel test section modification has been designed to allow isolated testing of the 1:4 scale custom propulsor (see Appendix A). A diffusing adaptor transforms the MIT 1'×1' square tunnel cross-section into a 15.625" diameter round section. Screens are used to reduce flow non-uniformities, boundary layer

growth and separation in the diffuser. The flowfield has been mapped by surveys using a stagnation pressure rake, and it is found that the non-uniformity in stagnation pressure is less than 15% of the mean dynamic pressure at that location.

6.2 Suggestions for Future Work

1. Additional 1:11 scale centerbody plugs and the 1:4 scale nacelle and plugs need to be designed once the requirements of the propulsors are completely determined.
2. Detailed design work and iteration of the custom propulsor mechanical design is needed to size fasteners and fillets, update the turbomachinery and nacelle to their final versions, and ensure compliance with NASA LaRC guidelines on factors of safety. A final decision must be made, in collaboration with NASA, regarding the rotor-shaft attachment scheme.
3. The proposed motor vibration test in Chapter 4 needs to be carried out. This is a necessary risk reduction item.
4. Additional investigation is required into the repeatability and uncertainty margins of the electric motor calibration, particularly at temperatures near 60°C. This may necessitate replacement of the load cell with one of higher accuracy and implementation of a better means of controlling motor temperature.

Appendix A

Appendix A: Design of a Diffusing Transition Duct

To determine fan characteristics in uniform flow and distortion, it is useful to test scale model propulsors in isolation. These isolated turbomachinery tests may be performed in a test section whose diameter matches that of the nacelle shroud with the fan, stator and hub used without the remainder of the nacelle or aircraft model.

The wind tunnel available at MIT for these tests is open-circuit with a 1'×1' test section, so an adaptor is needed which attaches downstream of the existing test section. An adaptor been designed and constructed for the 5.7 in. diameter 1:11 scale model fan. The adaptor has a square-to-round transition with an area ratio of $5.64:1$. The area contraction reduces flow non-uniformities and decreases boundary layer growth [35], simplifying the production of a uniform downstream flow.

For tests of the 15.625 in. diameter 1:4 scale fan, a diffuser with an area ratio of $1:1.33$ is required. The adverse pressure gradient in the diffuser increases the relative size and magnitude of flow non-uniformities as shown from the streamwise momentum equation,

$$u\frac{\partial u}{\partial x} = -\frac{1}{\rho}\frac{\partial p}{\partial x}\,. \tag{A.1}$$

In an adverse pressure gradient, flow with a higher initial velocity will be decelerated less than flows with a low initial velocity (boundary layers or wakes). From continuity, the greater deceleration of these wakes will also result in an increase in their relative size. This complicates the design of the required diffusing section, as does the transition from square-to-round cross-section, which can induce separation in the corners.

Screens can be used to suppress flow non-uniformities.[1] For areas of higher dynamic pressures the loss through the screen is greater than for the flow in wakes or boundary layers. There is thus a pressure gradient normal to the flow in the vicinity of the screen and streamline curvature both upstream and downstream of the screen. The higher velocity flow is diffused, and the lower velocity flow accelerated. It is possible for sufficiently high K values for the correction to outweigh the initial non-uniformity and the upstream velocity defect to result in a downstream velocity excess [35]. This may be seen in Fig. A-1, which shows data from traverses with a Kiel probe upstream and downstream of a screen with $K = 3$.

Screens have also been shown to reduce boundary layer separation in diffusers [36], and are thus helpful in the desired test section modification. A diffuser angle of $2\phi = 8°$ is selected based on Fig. A-2 from McDonald and Fox [37], where N/R_1 is the axial length of the diffuser normalized by the upstream hydraulic radius, equal to 4.2 for the chosen design. The selected length and angle lie below the line of first appreciable stall. Three screens with $K = 3$ and an axial spacing of $0.5D$ are used based on Fig. A-3 from Hancock [38] which shows the normalized modal amplitude u_N/u_0 of disturbances as a function of screen spacing and combined screen pressure drop coefficient ΣK. Our design corresponds to $pX = 3.14$ and $\Sigma K = 9$ (the curve labels on Fig. A-3 correspond to ΣK). The spacing is sufficient to aerodynamically de-couple the screens [35].

Data from the resulting design is shown in Fig. A-4, which indicates the screen locations and the results of cross-channel wake surveys with and without screens installed at each axial location. The evolution of the 95% boundary layer thickness, $\delta_{0.95}$ is given. The effect of the screens is to reduce $\delta_{0.95}$, which in this case is a

---

[1] Screens are typically described according to a screen pressure drop coefficient, K, defined as $K = \frac{\Delta p}{1/2 \rho u^2}$ where K is a constant which depends on the screen solidity. Various estimates for K as a function of solidity exist. For our purposes we will assume $K = 0.8s/(1-s)^2$ where s is the solidity [35].

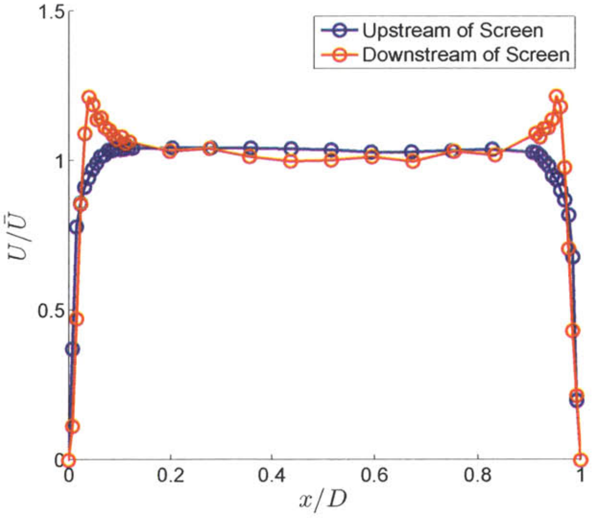

Figure A-1: Velocities in a round duct of diameter D, upstream and downstream of a screen with $K = 3$.

more appropriate measure of the boundary layer than the displacement thickness $\delta^* \equiv \int (1 - {}^{u}/_{u_\infty})\, dy$, which can become negative due to the effects of overshoot as in Fig. A-1. Fig. A-4 shows that the overshoot decays between screens, and that the reduction in the boundary layer thickness is cancelled by growth between screens, meaning that the addition of successive screens and the associated ducting past the first screen result in a negligible net change in $\delta_{0.95}$.

We are also interested in minimizing flow non-uniformities outside the boundary layer. Wake surveys carried out at each screen axial location are shown in Fig. A-5. In Fig. A-5(a), the wake from an upstream pitot probe installed in the right-hand wall of the tunnel is visible. Fig. A-5(b) indicates an area of separation in the upper right corner of the diffuser, the effects of which have been attenuated by the time the flow has passed through the second and third screens. There is approximately a 15% variation in stagnation pressure outside the boundary layer downstream of the last screen, which corresponds to 7% variation in velocity.

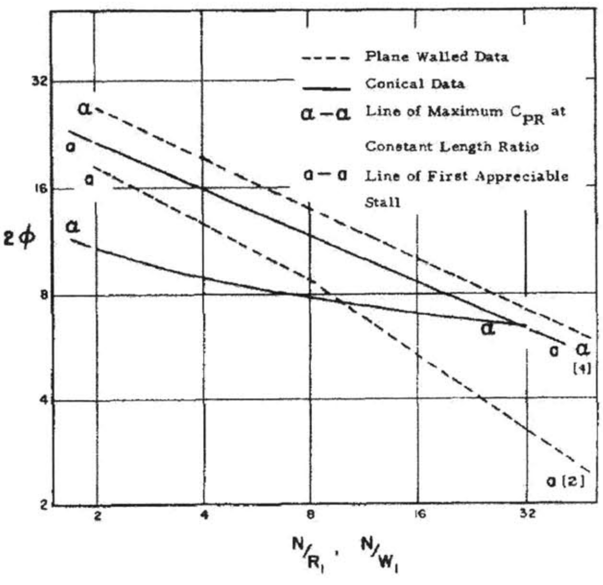

Figure A-2: Flow in a conical diffuser from Fox with the line of first appreciable stall denoted by 'a—a'. $^{N}/_{R_1} = 4.2$ and $2\phi = 8°$ for our diffuser.

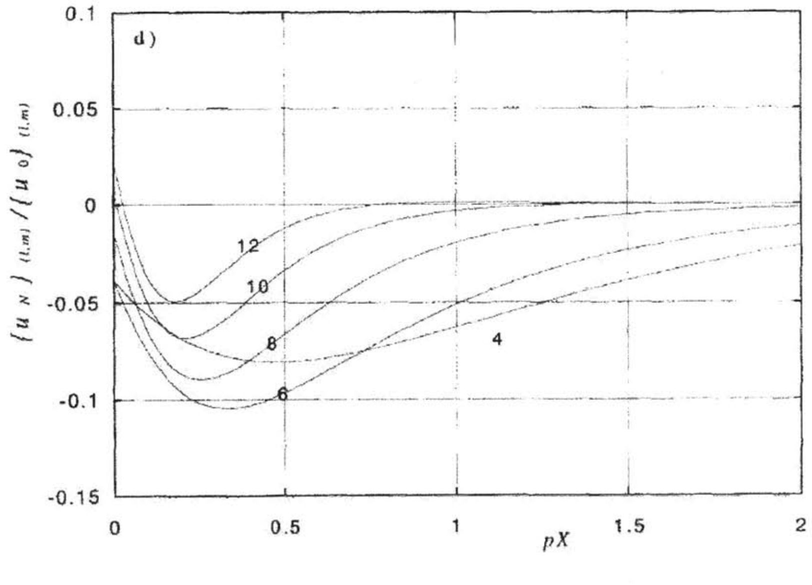

Figure A-3: Normalized disturbance amplitude as a function of screen spacing pX and total pressure drop coefficient ΣK (on curve labels) from Hancock. $pX = 3.14$ and $\Sigma K = 9$ for our adaptor.

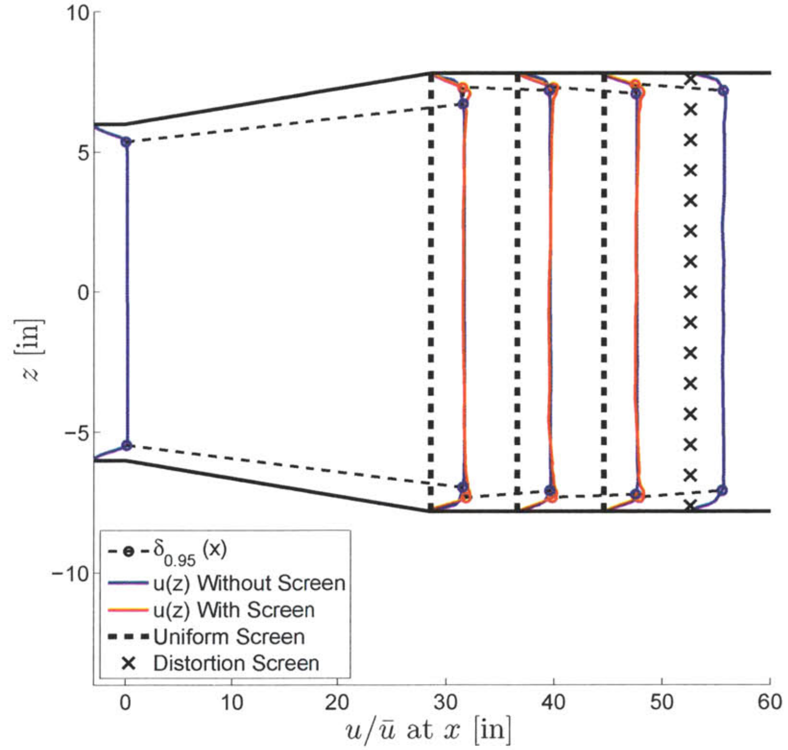

Figure A-4: Diffusing transition duct geometry, normalized velocity profiles and 95% boundary layer evolution.

The decay of the area-weighted disturbance magnitude $\mathcal{D}$, defined as

$$\mathcal{D} \equiv \sqrt{\frac{1}{A}\sum_{i=1}^{N} A_i \left(\frac{p_{t,i} - p_{ref}}{\bar{p}_t - p_{ref}} - 1\right)^2}, \tag{A.2}$$

is shown in Fig. A-6. $\mathcal{D}$ is reduced by successive screens despite $\delta_{0.95}$ remaining constant, indicating decay of non-uniformities outside the boundary layer, as can also be seen in Fig. A-5. Further benefit might be obtained by the use of additional screens, but there are constraints on the axial length of the adaptor for use with our wind tunnel.

The data show that the adaptor reduces flow non-uniformities to a level acceptable for isolated turbomachinery tests of the 1:4 scale propulsor. We will also assess the effect of operation in distortion by simulating the boundary layer on the upper fuselage of the 1:4 scale aircraft model. This can be accomplished with the use of a screen whose solidity varies across the height of the test section such as in Fig. A-7 (the center spar is intended to prevent warping or fluttering of the thin crossbars). The design shown in Fig. A-7 derives from the existing distortion screen used at the 1:11 scale, but has not yet been built or tested. Its intended axial location is noted in Fig. A-4.

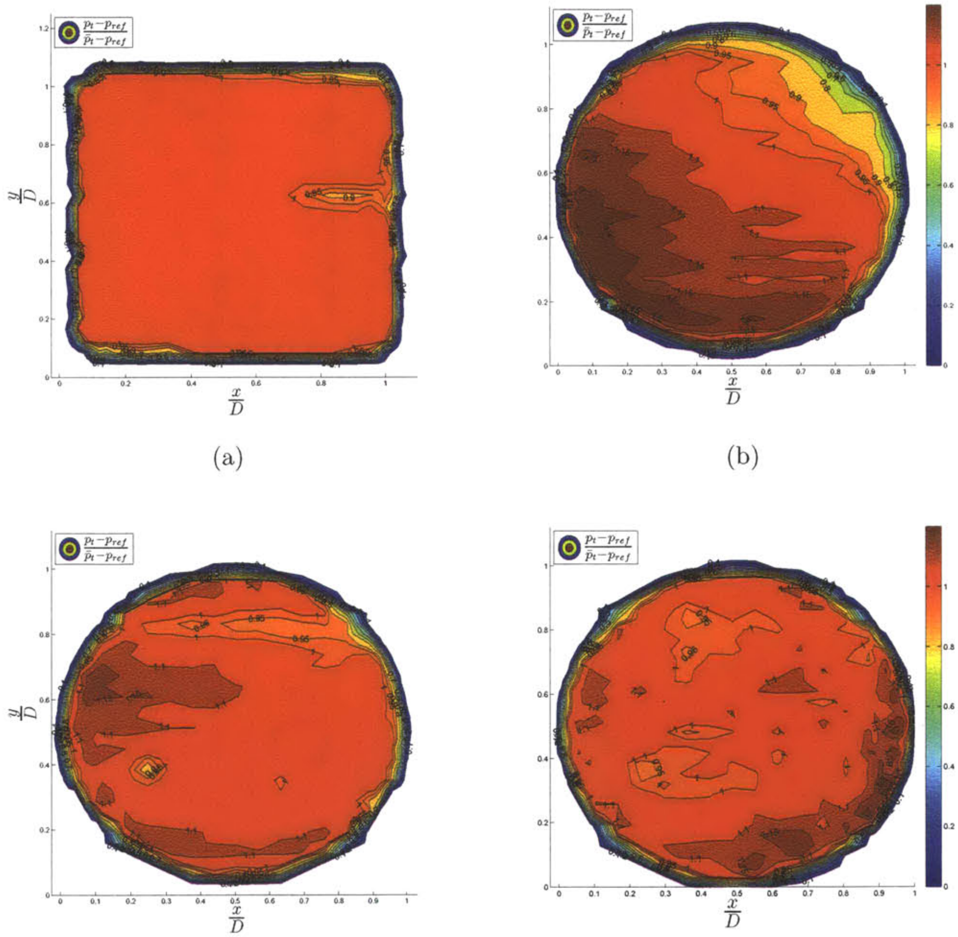

(a) (b)

(c) (d)

Figure A-5: Contours of normalized stagnation pressure: a) at 1'×1' tunnel exit; b) after diffuser and 1 screen; c) after diffuser and 2 screens; d) after diffuser and 3 screens.

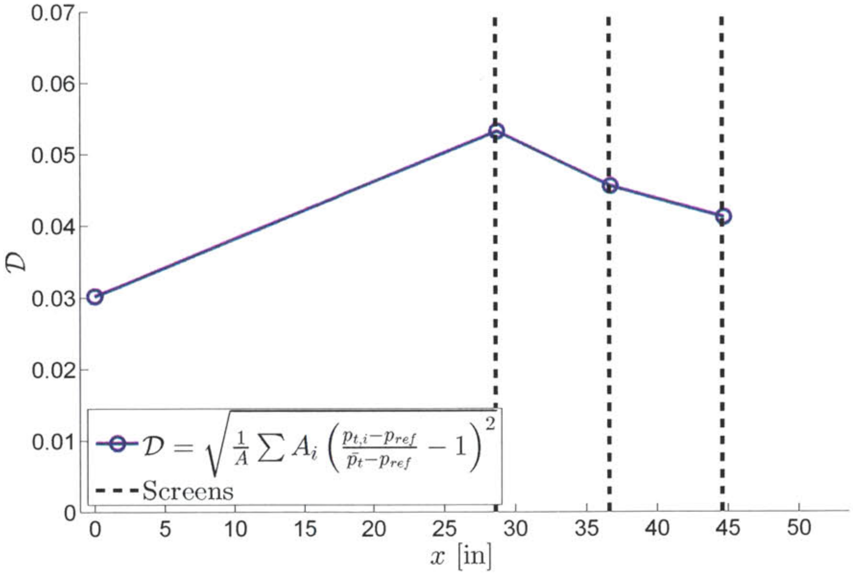

Figure A-6: Area-weighted disturbance magnitude evolution through the wind tunnel adaptor.

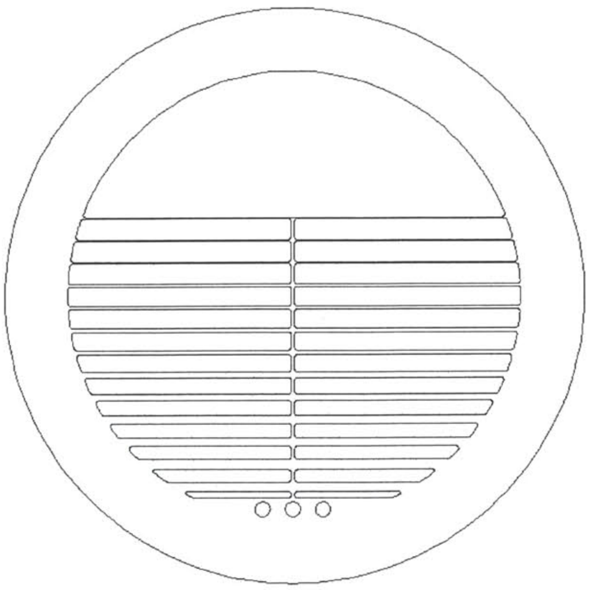

Figure A-7: Preliminary design for a 1:4 scale distortion-generating screen.

Bibliography

[1] Greitzer, E. M., et. al, "N+3 Aircraft Concept Designs and Trade Studies," Tech. Rep. CR-2010-216794/VOL1, NASA, 2010.

[2] Drela, M., "N+3 Aircraft Concept Designs and Trade Studies - Appendix," Tech. Rep. CR-2010-216794/VOL2, NASA, 2010.

[3] Drela, M., "Simultaneous Optimization of the Airframe, Powerplant, and Operation of Transport Aircraft," 2^{nd} *Royal Aeronautical Society Aircraft Structural Design Conference*, Hamilton Place, London, October 2010.

[4] Drela, M., "Development of the D8 Transport Configuration," 29^{th} *AIAA Applied Aerodynamics Conference*, Honolulu, HI, June 2011.

[5] Drela, M., "Power Balance in Aerodynamic Flows," 27^{th} *AIAA Applied Aerodynamics Conference*, San Antonio, TX, June 2009.

[6] Huang, A., Uranga, A., and Greitzer, E., "Assessment of BLI Benefits for Advanced Civil Aircraft," Gas Turbine Lab Seminar, 2013.

[7] Greitzer, E. M., "Aircraft and Technology Concepts for an N+3 Subsonic Transport: Proposal for Extension of Phase II Program," Tech. rep., NASA, 2013.

[8] Cumpsty, N., *Jet Propulsion*, Cambridge University Press, Cambridge, UK, 2nd ed., 2003.

[9] Greitzer, E. M., et. al, "Aircraft and Technology Concepts for an N+3 Subsonic Transport Phase II," Tech. rep., NASA, 2012.

[10] Lord, W. K., "Notes on Velocity Scaling and Propulsion Simulator Design," Internal project document, 2011.

[11] Papalambros, P. Y. and Wilde, D. J., *Principles of Optimal Design*, Cambridge University Press, Cambridge, UK, 2nd ed., 2000.

[12] NeuMotors, "Product specifications," Online, July 2013, www.neumotors.com.

[13] C. G. Kim, J. H. Lee, H. W. K. and Youn, M. J., "Study on Maximum Torque Generation for Sensorless Controlled Brushless DC Motor with Trapezoidal Back EMF," *IEE Journal*, Vol. 152, No. 2, March 2005, pp. 277–291.

[14] Moffitt, B. A., *A Methodology for the Validated Design Space Exploration of Fuel Cell Powered Unmanned Aerial Vehicles*, PhD dissertation, Georgia Institute of Technology, School of Aerospace Engineering, May 2010.

[15] High Performance Electric Vehicle Systems, "Product specification sheet," Online, July 2013, www.hpevs.com.

[16] Advanced Motors & Drives, "Product specification sheet," Online, July 2013, www.evparts.com.

[17] Çengel, Y. A., *Heat and Mass Transfer*, McGraw-Hill, New York, NY, 3rd ed., 2007.

[18] National Council of Examiners for Engineering and Surveying, *Fundamentals of Engineering Supplied-Reference Handbook*, NCEES, Clemson, SC, eighth ed., Oct. 2008.

[19] Lee, E. T. Y., "A Simplified B-Spline Computation Routine," *Computing*, Vol. 29, No. 4, 1982, pp. 365–371.

[20] Drela, M., *A User's Guide to MTFLOW 2.01*, MIT Aerospace Computational Design Laboratory, June 2010.

[21] Drela, M., "Aerodynamics of Viscous Flows," 2013, 16.13 course notes.

[22] The MathWorks, *MATAB*, R2009a ed., Feb. 2009.

[23] Drela, M., MIT. Personal communication, April 2013.

[24] TURBOCAM Int., "Request for Quote," Dec. 2012, www.turbocam.com.

[25] M. I. Friswell, J. E. T. Penny, S. D. G. and Lees, A. W., *Dynamics of Rotating Machines*, Cambridge University Press, Cambridge, UK, 2010.

[26] While, M. F., "Rolling Element Bearing Vibration Transfer Characteristics: Effect of Stiffness," *Journal of Applied Mechanics*, Vol. 46, 1979, pp. 677–684.

[27] Moffitt, B., UTRC. Personal communication, July 2012.

[28] Pansini, A. J., *Basics of Electric Motors*, Pennwell Publishing Company, Tulsa, OK, 2nd ed., 1996.

[29] Miller, T., *Brushless Permanent-Magnet and Reluctance Motor Drives*, Clarendon Press, Oxford, UK, 1989.

[30] Keesaman, J., Neumotors, Inc. Personal communication, 2013.

[31] Drela, M., "Second-Order DC Electric Motor Model," 2006, MIT Aero & Astro.

[32] Titchener, N., MIT. Personal communication, Aug. 2013.

[33] Omegadyne, Inc., *Subminiature Industrial Compression Load Cell: Model LCKD-10*, Sept. 2011.

[34] Siu, N., MIT. Personal communication, Aug. 2013.

[35] Greitzer, E. M., Tan, C. S., and Graf, M. B., *Internal Flow*, Cambridge University Press, New York, NY, 2004.

[36] Schubauer, G. B. and Spangenberg, W. G., "Effect of Screens in Wide-Angle Diffusers," Tech. Rep. 949, NACA, 1947.

[37] McDonald, A. T. and Fox, R. W., "An Experimental Investigation of Incompressible Flow in Conical Diffusers," *International Journal of Mechanical Sciences*, Vol. 8, 1966, pp. 125–139.

[38] Hancock, P. E., "Plane Multiple Screens in Non-Uniform Flow, with Particular Application to Wind Tunnel Settling Chamber Screens," *European Journal of Mechanics - B/Fluids*, Vol. 17, No. 3, 1998, pp. 357–369.